






A Novel Density Profile for Isothermal Cores of Dark Matter Halos

Vinh Tran ¹, Xuejian Shen ¹, Mark Vogelsberger ¹, Daniel Gilman ^{2,3}, Stephanie O’Neil ^{4,5} and Jiarun Gao⁶

¹*Department of Physics and Kavli Institute for Astrophysics and Space Research,
Massachusetts Institute of Technology, Cambridge, MA 02139, USA**

²*Department of Astronomy & Astrophysics, University of Chicago, Chicago, IL 60637, USA*
³*Brinson Prize Fellow*

⁴*Department of Physics & Astronomy, University of Pennsylvania, Philadelphia, PA 19104, USA*

⁵*Department of Physics, Princeton University, Princeton, NJ 08544, USA*

⁶*University of Rochester, 500 Joseph C Wilson Blvd, Rochester, NY 14627, USA*

(Dated: November 20, 2024)

We present a novel density profile for halos in self-interacting dark matter (SIDM) models, which accurately captures the flat- and isothermal-core configurations. We show analytically how our density profile satisfies these conditions, with comparisons to other contemporary functional choices. We demonstrate the versatility of our profile by putting it into the context of idealized N-body simulations and show that it provides excellent representations for both density and velocity dispersion structures of the simulation data. When an estimated fitting criterion is used to approximate the general cases, such as in cosmological simulations, the resulting regressions maintain their goodness of fit in both extremes, in the initial thermalization phase and the late core-collapse regime. Our density profile provides a framework for more detailed analyses of halos in different SIDM models while serving as the basis for reducing simulation needs and constructing initial conditions for deep core-collapse simulations.

I. INTRODUCTION

Despite the success of the Λ CDM (cosmological constant plus collisionless cold dark matter, CDM) model in explaining the large-scale structures of the universe [e.g. 1, 2], challenges remain in matching observations of small-scale structures [e.g. 3, 4], such as the core-cusp problem [e.g. 5, 6], the too-big-to-fail problem [7], or the problem of diversity of rotation curves [8, 9].

Self-interacting dark matter (SIDM) is an important class of DM models alternative to CDM and is well motivated by hidden sector models beyond the standard model [e.g. 10–12]. SIDM provides promising solutions to many of the small-scale problems [see e.g. a review of 13]. The elastic [14] collisions between DM particles result in the thermalization of the inner part of the halo and lead to the formation of cores [e.g. 15–17], which could explain the core-cusp and the too-big-to-fail problems. Meanwhile, the strong response of SIDM halo structure to halo concentration and baryon dominance results in more diverse rotation curves compared to the CDM case and is more aligned with observations [e.g. 8, 9, 18]. In recent years, SIDM with extremely large interaction cross-sections has gained popularity in explaining the dense compact substructures found in strong gravitational lensing observations [19]. In this regime, the efficient heat conduction and the negative heat capacity of the SIDM halo result in gravothermal collapse (e.g. [20–22]), and was originally discussed in the context of globular clusters, e.g. [23].

After the initial thermalization process and throughout the gravothermal collapse process [24], the central

density profile remains as an isothermal core. However, in the outer region of the halo, due to the decreased number density and velocity dispersion of DM particles, they barely interact once in the lifetime of the universe. Therefore, the density profile will eventually transition to the NFW profile [25] found in CDM simulations. Such behavior of SIDM density profiles has been found in cosmological and isolated N-body simulations [e.g. 15–17, 26, 27].

To characterize DM halos’ properties throughout their evolution, it is common to fit the density profiles with certain functional choices based on the plateaus of the density and velocity dispersion profiles at smaller radii. We denote these behaviors as the flat-core and isothermal-core configurations. Many of the analytical profiles currently used to describe halos in SIDM models utilize the NFW profile with modifications to achieve the flat-core configuration [28–31]. However, the aims of these profiles are restricted to approximately matching the density profile only. Because the performance of the velocity dispersions’ reconstructions is not taken into account, as we will show, common analytic descriptions of the halo profile typically do not reproduce the isothermal central cores seen in numerical simulations. When the commonly used models are used as a fitting function for the density profile, their failure to match the isothermal core configuration profile may not represent a serious issue. However, this limitation of existing models may impede progress in advancing the theoretical understanding of SIDM halo evolution because the parameters describing the density profile do not produce the isothermal solution that characterizes fully-thermalized SIDM halo cores.

Here, we present a novel density profile that closely approximates both the density and velocity dispersion structures of halos evolving with dark matter self-interactions. Section II details the different contempo-

* vinhtran@mit.edu

rary profile choices, as well as the motivation and derivation of our profile with the introduction of a criterion used to assess the approximation level to the isothermal-core configuration. Further analytical inspections and comparisons of our profile with others are presented. Section III inspects the fitting and reconstructing results of the profiles in the context of isolated N-body simulations. We conclude the investigation with the summary in Section IV and discuss potential further applications of the profiles in future SIDM studies.

II. ANALYTICAL DENSITY PROFILES

A. Flat-core Density Profiles

The NFW profile represents a stable configuration of halos in the CDM model observed in cosmological N-body simulations, following

$$\rho_{\text{NFW}}(r) = \frac{\rho_s}{(r/r_s)(1+r/r_s)^2}, \quad (1)$$

where, ρ_s and r_s are the scale density and radius. Two of the most commonly used modified profiles based on NFW are the Read ρ_{R16} [28] and the Robertson-Fischer $\rho_{\text{R17-F24}}$ profiles [29, 30].

The Read profile ρ_{R16} approximates the enclosed mass profiles of flat-core halos as

$$M_{\text{R16}}(r) = M_{\text{NFW}}(r) \tanh^\alpha(r/r_c), \quad (2)$$

Here, $M_{\text{NFW}}(r)$ is the NFW mass profile, r_c is the characteristic core radius, and α is an additional degree of freedom (DOF) controlling the flatness of the halo core, often taking the value of $\alpha = 1$. The characteristic core density ρ_c of the Read profile can be recovered from the corresponding NFW scale density ρ_s as $\rho_c = 1.5\rho_s r_s/r_c$. It must be noted here that the scale density and radius of the Read profile are not necessarily the same as the initial NFW parameters, and their values can change throughout the evolution of the halo.

The Robertson-Fischer profile, on the other hand, approximates the flat-core configuration with a power-law modification

$$\rho_{\text{R17-F24}}^*(r) = \frac{\rho_c}{\left(1 + (r/r_c)^\beta\right)^{1/\beta} (1 + r/r_s)^2}, \quad (3)$$

with $\beta \in [2; 4]$ fixed. This power-law, often taking the value of $\beta = 4$, ensures that the density profile converges almost perfectly to the NFW profile for all radii larger than the core radius. A clear problem of the Robertson-Fischer and Read profiles' approach is the assignment of the inverted power-law index n to the value of $n = 1$ within the halo intermediate region (defined as the region between the flat-core and the halo edge where $\rho \propto r^{-3}$). This differs significantly from the value of $n = 2.19$ in

the self-similar analytical calculation [22], as well as values measured in simulations, which also vary throughout the halo evolution as shown later in Section III C [?]. Accommodating this variation requires the Robertson-Fischer profile to increase the number of DOFs, taking the form

$$\rho_{\text{R17-F24}}(r) = \frac{\rho_c}{\left(1 + (r/r_c)^\beta\right)^{n/\beta} (1 + r/r_s)^{3-n}}. \quad (4)$$

The Read profile, involving the NFW mass profile, is more troublesome to modify. We instead refer to the more straightforward approach of the Yang profile ρ_{Y23} [27] which utilizes a triple power-law to approximate the DM halo structure,

$$\rho_{\text{Y23}}(r) = \frac{\rho_c}{1 + (r/r_c)^n (1 + r/r_s)^{3-n}}. \quad (5)$$

We expect DM halos to behave somewhat self-similarly as described by [22, 23] in the LFMP limit, where the mean distance between DM collisions λ_{col} is much larger than the system's gravitational scale height H_{grav} , which is often reasonably assumed throughout much of the halo evolution. This self-similarity means that at different epochs of the gravothermal collapse, the inner regions of halos exhibit roughly the same structure when properly scaled, following the self-similar solution. A clear indication of such behaviors is the stability of n at different epochs, hinting at the importance of measuring n rather than fixing it to certain values.

B. Isothermal-core Density Profile

Building on the flat-core approach taken by the Read, Robertson-Fischer, and Yang profiles, we investigate different analytical trial functions $\rho(r)$ that, in addition to satisfying the flat-core configuration, can closely approximate an isothermal core. We require the density profile to exhibit a similar density structure to that mentioned in Section II A: having a radius-independent density at lower radii, an inverted power-law of n in the intermediate region, and a power-law of r^{-3} similar to the NFW profile at the halo edge. To characterize the level of isothermality (defined as closeness of the system to the isothermal-core configuration), we start with the spherically symmetric Jeans equation

$$\frac{\partial}{\partial r} \left[\rho(r) \sigma_r^2(r) \right] = -\rho(r) \frac{GM(r)}{r^2}. \quad (6)$$

We then employ a technique similar to the approach taken in [18, 32]. However, rather than setting the velocity dispersion across the whole isothermal core to a single constant value of $\sigma_r(r) = \sigma_c$, we take a more localized approach and allow $\sigma_r(r)$ to be a piecewise constant function. This means that within the interval $[r - \Delta r, r + \Delta r]$ for $dr \ll \Delta r \ll r_c$, $\sigma_r(r) = \sigma_c(r) \approx$

Density Profile	N_{DOF}	Behavior in Different Regions			Analytical Form
		$r \ll r_c$	$r_c \ll r \ll r_s$	$r_s \ll r$	
ρ_{R16}	3	$\rho \propto \text{const}$	$\rho \propto r^{-1}$	$\rho \propto r^{-3}$	$\frac{2}{3}\rho_c \left[\frac{\tanh r/r_c}{r/r_c} \frac{1}{(1+r/r_s)^2} + \left(\frac{\text{sech } r/r_c}{r/r_s} \right)^2 \left(\ln \left(1 + \frac{r}{r_s} \right) - \frac{r/r_s}{1+r/r_s} \right) \right]$
$\rho_{\text{R17-F24}}$	4	$\rho \propto \text{const}$	$\rho \propto r^{-n}$	$\rho \propto r^{-3}$	$\rho_c / \left[\left(1 + (r/r_c)^4 \right)^{n/4} (1 + r/r_s)^{3-n} \right]$
ρ_{Y23}	4	$\rho \propto \text{const}$	$\rho \propto r^{-n}$	$\rho \propto r^{-3}$	$\rho_c / \left[1 + (r/r_c)^n (1 + r/r_s)^{3-n} \right]$
ρ_{T24}	4	$\rho \propto \text{const}$	$\rho \propto r^{-n}$	$\rho \propto r^{-3}$	$\rho_c \left(\frac{\tanh r/r_c}{r/r_c} \right)^n / \left[\left(1 + (r/r_s)^2 \right)^{(3-n)/2} \right]$

TABLE I. Summary of analytical density profiles. $\alpha = 1$, $\beta = 4$, and $\gamma = 2$ are set for ρ_{R16} , $\rho_{\text{R17-F24}}$, and ρ_{T24} , respectively.

const. The aforementioned dr is the differential interval for $\partial\rho(r)/\partial r$ and $\partial M(r)/\partial r$. This essentially sets $\partial\sigma_r(r)/\partial r = \partial\sigma_c(r)/\partial r = 0$ while allowing other derivatives to have non-trivial values. The trial function $\rho(r)$ is then used to calculate $\sigma_c(r)$. For an analytical profile that closely approximates the isothermal-core configuration, the resulting $\sigma_c(r)$ would satisfy $\sigma_c(r) \approx \text{const}$ for $\Delta r \sim r_c$. Non-dimensionalizing the Poisson and Jeans equations with $\bar{r} = r/r_c$ and $\bar{\rho}(\bar{r}) = \rho(r)/\rho_c$, we obtain the following equations

$$\frac{\partial \bar{M}(\bar{r})}{\partial \bar{r}} = \bar{r}^2 \bar{\rho}(\bar{r}), \quad (7)$$

$$\frac{\partial \bar{\rho}(\bar{r})}{\partial \bar{r}} = -\frac{1}{I(\bar{r})} \frac{\bar{\rho}(\bar{r}) \bar{M}(\bar{r})}{\bar{r}^2}. \quad (8)$$

Here, $\bar{M}(\bar{r}) = M(r)/4\pi r_c^3 \rho_c$ and $I(\bar{r}) = \sigma_c^2(r)/4\pi G \rho_c r_c^2$ with $I(\bar{r}) \approx \text{const}$ within the interval $[r - \Delta r, r + \Delta r]$. $I(\bar{r})$ can be thought of as the core kinetics-gravitational (K-G) ratio assuming isothermality, and rather than calculating $\sigma_c(r)$, we calculate

$$I(\bar{r}) = \frac{-\bar{\rho}^3 \bar{r}}{2\bar{\rho} \partial \bar{\rho} / \partial \bar{r} - \bar{r} (\partial \bar{\rho} / \partial \bar{r})^2 + \bar{r} \bar{\rho} \partial^2 \bar{\rho} / \partial \bar{r}^2}. \quad (9)$$

Testing different trial functions, we notice a specific density profile resulting in a core isothermal K-G ratio approaching a radius-independent form at $r \lesssim r_c$ with $n \sim 2.0$ – 2.5 . The density profile, the analytical analysis of which is detailed in Appendix A, takes the form of

$$\rho_{\text{T24}}^*(r) = \rho_c \left(\frac{\tanh r/r_c}{r/r_c} \right)^n. \quad (10)$$

Including the necessary modifications to satisfy the density structure requirements, we introduce our density profile ρ_{T24}

$$\rho_{\text{T24}}(r) = \rho_c \left(\frac{\tanh r/r_c}{r/r_c} \right)^n \frac{1}{(1 + (r/r_s)^\gamma)^{(3-n)/\gamma}}. \quad (11)$$

Here, γ functions similar to the nuisance parameter β in the Robertson-Fischer profile $\rho_{\text{R17-F24}}$; however, rather

than controlling the sharpness of the core, γ regulates the transitioning between the intermediate region and the outer edge. We find that the best results are provided by $\gamma \geq 2$ with the detailed explanation presented in Appendix A. Onward, we set $\gamma = 2$ for our analysis. Similar adjustments can also be made for other profiles. However, we find that such modifications have no significant impact on the fitting or isothermality of the profiles. From Equation A13, we also retrieve the approximate core velocity dispersion of our profile, following

$$\sigma_{c,\text{T24}} = \sqrt{\frac{4\pi G \rho_c r_c^2}{2n + 3(3-n)\lambda^2}}. \quad (12)$$

This approximation, by its derivation, is only intended to work in the $r \ll r_c$ limit. However, as demonstrated in subsequent sections, the value of $\sigma_{c,\text{T24}}$ approximates the halo isothermal core's velocity dispersion surprisingly well, even at larger radii, up to a few of r_c . Table I summarizes the characteristics of the analytical density profiles under inspection.

C. Density Profiles Analysis

Figure 1 shows density structures of the Read profile ρ_{R16} , the modified Robertson-Fischer profile (hereafter referred to as the Robertson-Fischer profile) $\rho_{\text{R17-F24}}$, the Yang profile ρ_{Y23} , and our profile ρ_{T24} . Densities are normalized as $\bar{\rho} = \rho/\rho_c$ and shown as functions of the normalized radius $\bar{r} = r/r_c$. There are 3 choices of edge-core ratios, $r_s/r_c = 3, 10, 30$, and 3 choices of the intermediate region's inverted power-law index, $n = 1, 1.75, 2.5$ (for $\bar{\rho}_{\text{R16}}$ we include 3 choices of core flatness $\alpha = 0.5, 0.75, 1.0$ instead of n). As expected from their constructions, all profiles show similar morphology, with the exception of the Read profiles being limited by their DOFs. In the Yang profile and in our profile, we observe the dominant influence of n on the transitioning characteristics between the halo core and the intermediate region. The effects of r_s on the relevant areas diminish with increasing value of n , leading to the structures of the inner regions of halos with the same

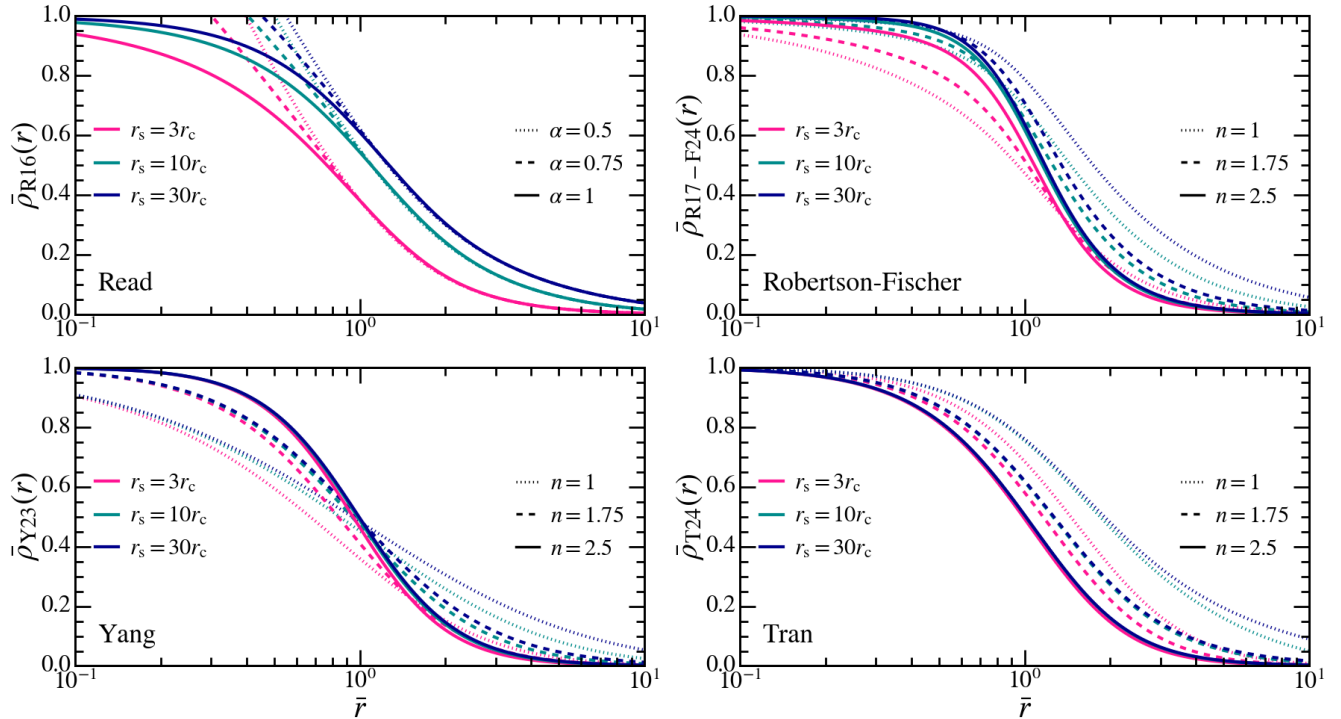


FIG. 1. The density profiles of the Read (top left), Robertson-Fischer (top right), Yang (bottom left), and our (bottom right) profiles. Densities and radii are scaled with the characteristics core density ρ_c and core radius r_c . Each profile family is shown with three choices of $r_s/r_c = 3, 10, 30$ (in pink, green, and blue) and three choices of $n = 1, 1.75, 2.5$, or $\alpha = 0.5, 0.75, 1.0$ for the Read profiles (in dotted, dashed, and solid lines).

value of n remain similar even when different values of r_s are exhibited.

Figure 2 shows the normalized velocity dispersion profiles $\bar{\sigma}_r = \sigma_r / \sqrt{G\bar{\rho}_c\bar{r}_c^2}$ reconstructed from Figure 1's density profiles using the spherically symmetric Jeans equation (Equation 6). For the Robertson-Fischer and Yang profiles, the velocity dispersion profiles with higher values of n approach the isothermal-core configuration, albeit with rough core transitioning behaviors. These behaviors, however, are not exhibited in our profile's velocity dispersions, resulting in the observed smoother transitions. The sub-panels in Figure 2 show the core isothermal K-G ratio at different radii for each examined profile. Those of the Robertson-Fischer profile depend strongly on radius, hinting at the strong deviation of the functional form from the isothermal-core configuration. Similarly, the Read and Yang profiles also deviate strongly from the conditions of an isothermal core, albeit to a lesser extent. Nevertheless, there appears to be a hint of specific parameter choices (with $n \sim 2.0\text{--}2.4$) of the Yang profile resulting in a higher level of isothermality. For our density profile, the resulting core isothermal K-G ratios consistently approach radius-independent configurations, with the values at lower radii correctly predicted by Equation A13. Surprisingly, the resulting core isothermal K-G ratios from our density profile's completed form $\rho_{T24}(r)$ (Equation 11) perform even better than those

calculated using the simplified version $\rho_{T24}^*(r)$ (Equation 10), the results of which are shown in the figure of Appendix A.

To better quantify the level of isothermality in each profile across parameter combinations, we derive the core isothermal mean-square deviation

$$\left\langle \left(\frac{\partial I}{\partial r} \right)^2 \right\rangle = \int_0^{r_c} \frac{4\pi\rho(r)r^2 dr}{M(r_c)} \left(\frac{\partial I(r)}{\partial r} \right)^2. \quad (13)$$

This deviation concerns the shell masses-weighted average of the core isothermal K-G ratio's deviation from the radius-independent conditions (reflected in the ratio's first derivative). Here, the normalizing factor $M(r_c)$ is taken as the enclosed mass at the core radius. Figure 3 shows the core isothermal mean-square deviations of the Robertson-Fischer, the Yang, and our profiles across a wide range of parameter combinations. The bottom left corner regions of all profile panels ($n \simeq 1; r_s \simeq r_c$) show a high level of isothermality. This is where the profiles essentially revert back to the modified NFW distribution with a flat core at the scale radius. The high level of isothermality is due to the fact that the NFW velocity dispersion profile peaks at r_s , which in the aforementioned cases where $r_c \sim r_s$, causes the core to appear isothermal. The values of the deviations in these regions can serve as the benchmark for the level of isothermal-

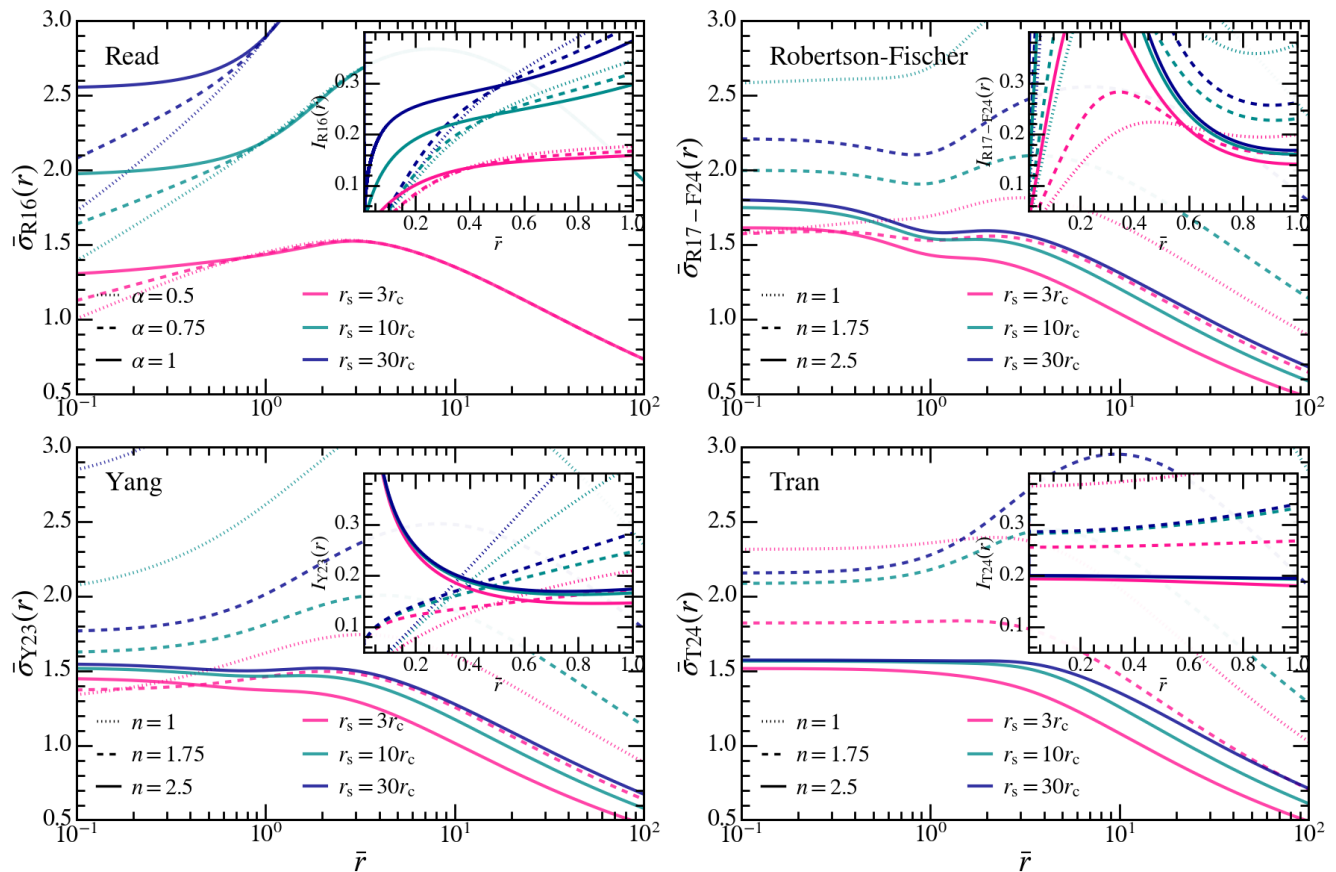


FIG. 2. The velocity dispersion profiles reconstructed from the density profiles presented in Figure 1 using the spherical symmetric Jeans equation (Equation 6). Velocity dispersions and radii are scaled with $\sqrt{G\rho_c r_c^2}$ and r_c . Again, the Read (top left), Robertson-Fischer (top right), Yang (bottom left), and our (bottom right) profiles are shown with three choices of $r_s/r_c = 3, 10, 30$ (in pink, green, and blue) and three choices of $n = 1, 1.75, 2.5$, or $\alpha = 0.5, 0.75, 1.0$ for the Read profiles (in dotted, dashed, and solid lines). The sub-panels show the respective core isothermal K-G ratios following from Equation 9 for the halo most inner region $r \leq r_c$.

ity. With such observations aside, we focus on other behaviors of the different profiles. The Robertson-Fischer profile appears to be the most limited, with higher levels of isothermality only occurring at lower values of the edge-core ratios. For the Yang profile, we observe the existence of an optimal parameter combination region, located within a narrow strip centering around the value of $n \approx 2.15$, near the calculated value in the self-similar analytical calculation [22]. Interestingly, there also exists an optimal parameter space centering at $n \approx 2.20$ for our density profile. However, this region reaches a significantly higher level of isothermality and skews more towards higher values of the edge-core ratio. Additionally, although the highest level of isothermality resulting from our profile remains localized around the value of $n \approx 2.20$, a large range of n can still accommodate close approximation to the isothermal-core configuration.

III. APPLICATION TO SIDM HALOS IN SIMULATIONS

A. Simulation Data

In order to evaluate and compare the utility of the density profiles, we assess them in the context of numerical simulations. Here, we make use of the high-resolution N-body simulations of isolated DM halos presented in [33] and [34]. Each of the halos in these data sets contains 3×10^7 DM particles within the virial radius and is initialized with the NFW configuration. These simulations use velocity-independent cross section (VICS) models as well velocity-dependent resonant cross section models. However, we focus on the VICS simulations and evaluate how well different forms of density profiles can describe the self-similar gravothermal collapse process of SIDM halos.

The first data set contains simulations of DM halos with mass $M_{200} = 10^{7.9} M_\odot$ and concentration parameter $c \simeq 18.7$. These halos have initial NFW scale den-

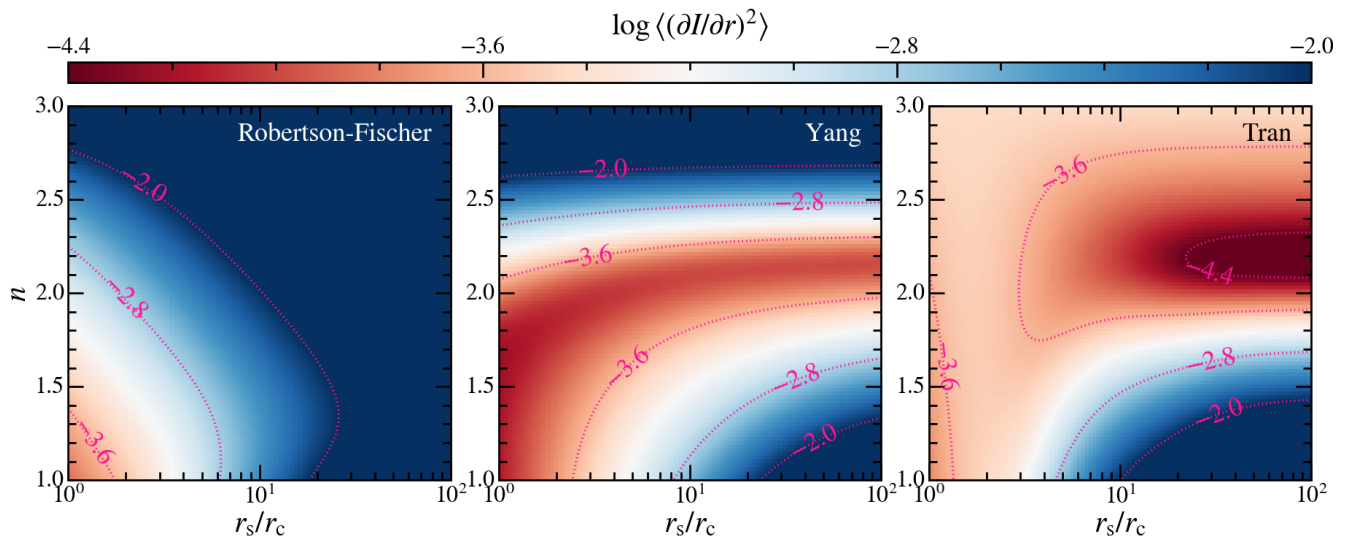


FIG. 3. The core isothermal mean-square deviations of the Robertson-Fischer (left), Yang (center), and our (right) profiles across a wide range of probable parameter choices. The edge-core ratios and intermediate region’s inverted power-law indices are varied in the range of $[10^0; 10^2]$ and $[1; 3]$, respectively. The color maps show values of the core isothermal mean-square deviations in log scale with contours indicating regions of $\log \langle(\partial I/\partial r)^2\rangle = -2.0, -2.8, -3.6, -4.4$.

sity and radius $\rho_s = 10^{7.43} M_\odot \text{ kpc}^{-3}$ and $r_s = 0.49 \text{ kpc}$. Two velocity-independent cross section for DM self-interactions are used in this data set; however, we focus mainly on the lower value of $\sigma/m = 31.98 \text{ cm}^2 \text{ g}^{-1}$ to avoid numerical effects causing deviation in the self-similarity [35–37]. The second data set contains a larger set of DM halo simulations, with the halo virial masses ranging from $10^{6.5} M_\odot$ to $10^{9.5} M_\odot$. The detailed configurations for the relevant simulations in the larger data set are presented in Appendix C.

B. Inference Algorithm

The particle counts within each simulation snapshot are measured using 100 log-spaced radial bins (hereafter referred to as shells) from $0.01 r_{s,\text{NFW}}$ to $3c r_{s,\text{NFW}}$, i.e. from around the value of the gravitational softening length to the largest sampling radius of the initial conditions at snapshot 0. The data are then further processed by merging shells with low particle counts and keeping only those within the virial radius $r_{200} = c r_{s,\text{NFW}}$, avoiding the strong exponential cut-off in place of the power-law $\rho \sim r^{-3}$ for $r > r_{200}$ in the initial conditions. We limit the number of DM particles per shell to at least 400, ensuring the minimum signal-noise ratio of $\text{SNR} \geq 20$.

To ensure proper statistics when fitting the density profiles to simulation data, we utilize the maximum likelihood method with Poisson statistics similar to the approach taken in [30]. The likelihood takes the form

$$\mathcal{L}(\boldsymbol{\theta}) = \prod_i \frac{\lambda_i(\boldsymbol{\theta})^{N_i} \exp^{-\lambda_i(\boldsymbol{\theta})}}{N_i!}. \quad (14)$$

Here, N_i is the particle count within radial bin (i.e. shell) i measured from simulations. $\lambda_i(\boldsymbol{\theta})$ is the expected value of N_i calculated from the density profile with the parameter combination $\boldsymbol{\theta} = (\rho_c, r_c, r_s, n)$. $\lambda_i(\boldsymbol{\theta})$ following

$$\lambda_i(\boldsymbol{\theta}) = \frac{1}{m_{\text{DM}}} \int_{r_i}^{r_{i+1}} 4\pi\rho(r, \boldsymbol{\theta})r^2 dr, \quad (15)$$

with m_{DM} as the mass of a DM particle. Maximizing the likelihood $\mathcal{L}(\boldsymbol{\theta})$ is equivalent to minimizing the negative log-likelihood (NLL), or when N_i is sufficiently large, to minimizing the residual sum of squares (RSS) $\chi^2(\boldsymbol{\theta}) = -2 \log \mathcal{L}(\boldsymbol{\theta}) + C = \sum_i (N_i - \lambda_i(\boldsymbol{\theta}))^2 / \lambda_i(\boldsymbol{\theta})$. Commonly, however, the density structure fit is performed with the logarithm of the density profile, in which case, the RSS would take the form of $\chi^2(\boldsymbol{\theta}) \simeq \ln^2(10) \sum_i (\log \rho_i - \log \hat{\rho}_i(\boldsymbol{\theta}))^2 / \text{SNR}_i^2$, with $\rho_i = 3N_i m_{\text{DM}} / 4\pi(r_{i+1}^3 - r_i^3)$ and $\hat{\rho}_i(\boldsymbol{\theta}) = \rho((r_{i+1} + r_i)/2, \boldsymbol{\theta})$. Here, we are taking $\Delta \log \rho_i \simeq \text{SNR}_i / \ln(10)$ and assuming the variation of the density within each bin as negligible. For measurements dominated by Poisson uncertainties, such as in idealized isolated halos, $\text{SNR}_i = \sqrt{N_i}$, resulting in

$$\chi_{\text{ideal}}^2 = (\boldsymbol{\theta}) \sum_i N_i (\log \rho_i - \log \hat{\rho}_i(\boldsymbol{\theta}))^2. \quad (16)$$

An immediate issue arises from the optimization of this RSS. The algorithm will tend to prioritize the outer regions’ regression over the halo core’s, where typically, only ~ 0.01 of the total number of particles reside. This leads to the core being poorly explained by the fitting, especially in the earliest and latest epochs of the halo evolution. In more general cases (such as in cosmological simulations) other sources of error contribute strongly to

the uncertainty, and as a consequence, Equation 16 becomes inadequate, and the aforementioned general form of $\chi^2(\boldsymbol{\theta})$ is required. To represent these cases with our simulation data sets, we assume uniform SNR across all shells, leading to

$$\chi_{\text{cosmo}}^2(\boldsymbol{\theta}) \propto \sum_i (\log \rho_i - \log \hat{\rho}_i(\boldsymbol{\theta}))^2. \quad (17)$$

We perform the density structure fits using both $\chi_{\text{ideal}}^2(\boldsymbol{\theta})$ and $\chi_{\text{cosmo}}^2(\boldsymbol{\theta})$ with the proportional factors set to $1/\sum_i N_i$ and $1/\sum_i 1$, respectively. To ensure numerical stability and convergence of the optimization algorithm (gradient descent methods in our case), we normalize the fitting parameters with the NFW scale density $\rho_{\text{s,NFW}}$ and scale radius $r_{\text{s,NFW}}$. Additionally, we utilize choose the initial parameters of $\boldsymbol{\theta}_{\text{init}} = (\rho_{\text{core}}/\rho_{\text{s,NFW}}, 1, 1, 2.5)$, with ρ_{core} as the approximate core density obtained via the algorithm detailed in Appendix B.

C. Fitting Results

For our analysis, we scale all radii, densities, and velocity dispersions with $r_{\text{s,NFW}}$, $\rho_{\text{s,NFW}}$, and $\sigma_{\text{s,NFW}} = \sqrt{G \rho_{\text{s,NFW}} r_{\text{s,NFW}}^2}$, while times are scaled with the collapse timescale t_{col} , defined in Equation 2.2 of [31] as

$$t_{\text{col}}(\sigma_{\text{eff}}/m) = \frac{150}{C} \frac{1}{\sigma_{\text{eff}}/m} \frac{1}{\rho_{\text{s,NFW}}} \left(\frac{1}{4\pi \sigma_{\text{s,NFW}}^2} \right)^{1/2}. \quad (18)$$

In the current picture, $C = \mathcal{O}(1)$ often takes the value of $C \simeq 0.75$ to match the result of fluid models [e.g. 27, 38, 39] and N-body simulations [e.g. 38, 40–42]. Here, we use the value of $C \simeq 0.85$ in order to approximate t_{col} as the onset of the gravothermal catastrophe, i.e. when the core density and velocity dispersion rapidly diverge while the core radius (and mass) vanishes. Nevertheless, for comparison purposes, analyses utilizing different values of C can easily be mapped to each other. The choice of σ_{eff}/m in Equation 18 is irrelevant to our results as we only look at halos in VICS models.

Figure 4 shows the density profile fits and the velocity dispersion reconstructions for a typical snapshot in the core collapse phase, where self-similarity is most relevant. We observe that all profiles perform well in representing the density and velocity dispersion structures of the outer regions. However, as predicted in Section III B, the halo core presents a much more significant challenge to reconstruct. For the Yang profile and our profile, we observe the density fits achieving high levels of representativeness to the simulation data, regardless of RSS choice. For other profiles (Read and Robertson-Fischer), utilizing the generalized RSS χ_{cosmo}^2 results in significantly better density fits and velocity dispersion reconstructions than when the idealized RSS χ_{ideal}^2 is employed.

The density profile fractional residuals $\delta_{\rho_i} = (\rho_i - \hat{\rho}_i)/\rho_i$ provide additional evidence for these arguments.

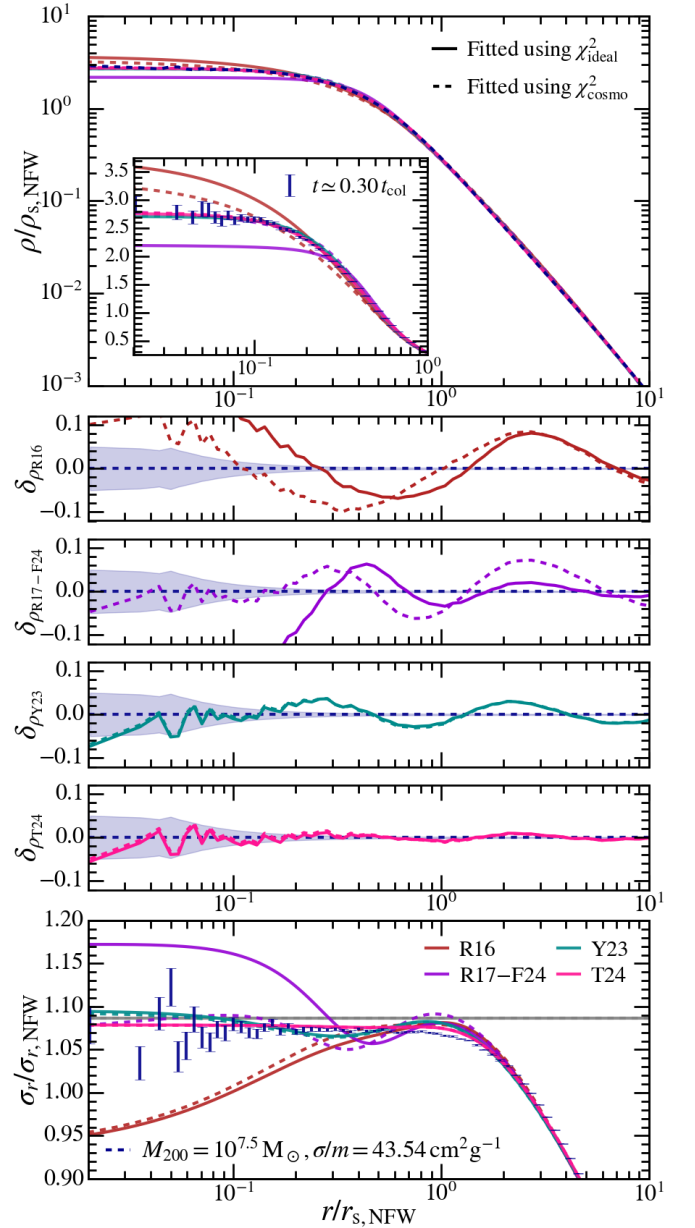


FIG. 4. Top: The density profile fits for a single snapshot at $t \simeq 0.30 t_{\text{col}}$ of the $10^{7.5} M_{\odot}$ halo evolved under the VICS of $\sigma/m = 43.54 \text{ cm}^2 \text{ g}^{-1}$. Fits utilizing ρ_{R16} , $\rho_{\text{R17-F24}}$, ρ_{Y23} , and ρ_{T24} are shown in brown, purple, cyan, and pink, respectively. Both RSSs (χ_{ideal}^2 and χ_{cosmo}^2) are optimized with the resulting profiles shown in solid and dashed lines. The main panel displays the fit in log scale, while the sub-panel shows a zoom-in of the core and intermediate region in linear scale. Simulation data are represented by a dashed blue line in the main panel and by blue error bars in the sub-panel. Middle: The 4 intermediate panels show the fractional residuals for the density profile fits. The blue dashed lines and filled regions represent the exact match to simulation data and Poisson uncertainties. Bottom: Comparison of simulation data (represented by blue error bars) to the velocity dispersions reconstructed from the regressed density profiles (using the spherically symmetric Jeans equation). The two horizontal gray lines show the core velocity dispersions calculated from Equation 12 and the ρ_{T24} regressed parameters. All quantities are scaled as described in Section III C.

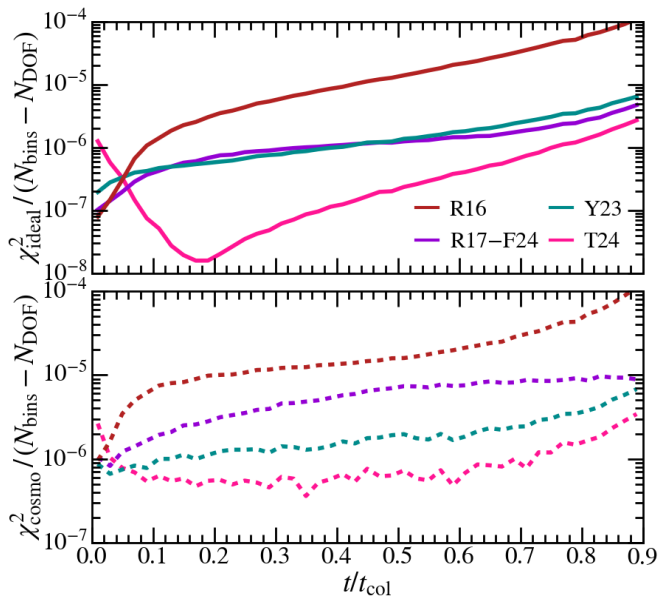


FIG. 5. Evolutions of the reduced χ_{ideal}^2 (top, solid) and χ_{cosmo}^2 (bottom, dashed) optimized utilizing ρ_{R16} (brown), $\rho_{\text{R17-F24}}$ (purple), ρ_{Y23} (cyan), and ρ_{T24} (pink). χ_{ideal}^2 and χ_{cosmo}^2 are calculated from Equation 16 and 17 with the proportion factors set to $1/\sum_i N_i$ and $1/\sum_i 1$, respectively. The resulting minimized RSSs are reduced over $N_{\text{bins}} - N_{\text{DOF}}$, with N_{bins} as the number of fitting bins (or shells) and N_{DOF} as the prior's number of DOF. Times are scaled as described in Section III C.

Two important features exhibited here are the goodness of fit with respect to the halo core and the fluctuation's amplitude occurring at the outer regions. The former indicates how well the inferred profile represents the halo core's density structure. The latter is the result of the mismatch between the regressed profiles' power-laws and the halo's actual density structure. This reflects the deviations of $r_{\text{s,NFW}}$ and n from the most appropriate values exhibited in the simulation data. From these features, we observe that although when χ_{cosmo}^2 is used, both the Robertson-Fischer, the Read, and the Yang profiles can provide excellent representations of the halo core, only with our profile is the outer regions also well approximated.

This translates to our profile having a better reconstruction of the velocity dispersion profile. A more detailed look shows the Yang and the Robertson-Fischer profiles following the simulation closely, albeit with certain suboptimal features deviating from the isothermal-core configuration, namely the wiggling inside the core and the rough transitioning behaviors. Parallel to the observation in Figure 2, for our profile, no such features exist, and the simulation data is almost exactly matched. The core velocity dispersions approximated by Equation 12 also provide a close estimation of the inferred value from the simulation data, with deviation only of the order of $\lesssim 1\%$.

Even at the earliest and latest snapshots (more de-

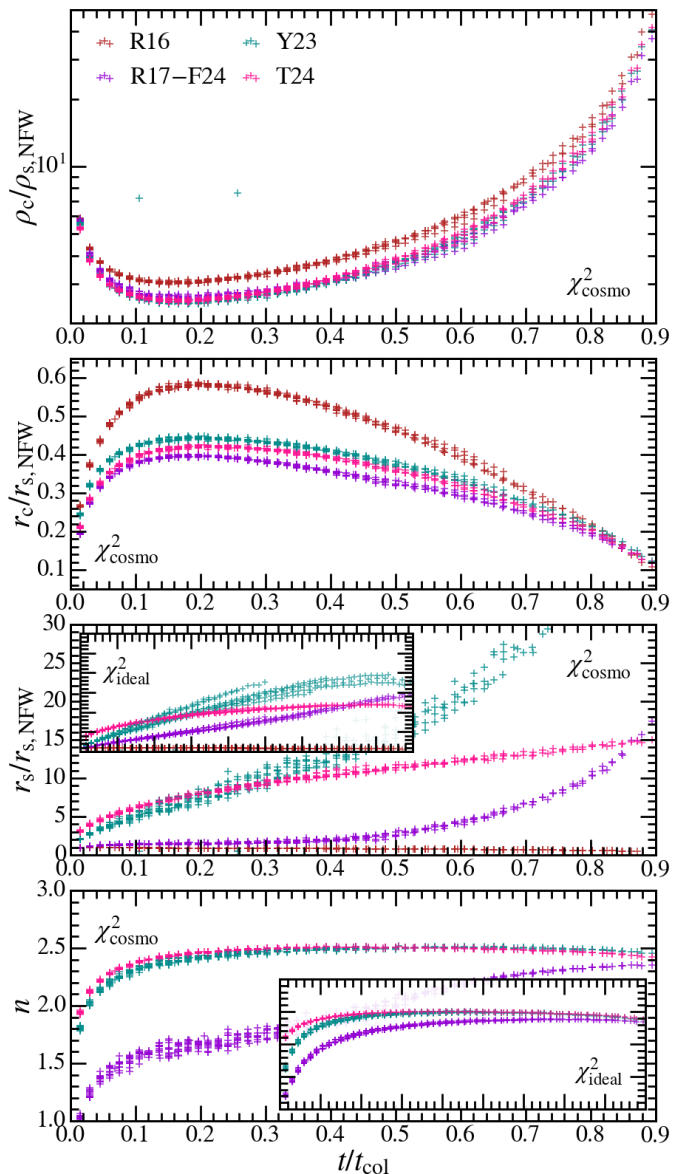


FIG. 6. The evolutions of the regressed core density ρ_c (top-most), core radius r_c (second-down), scale radius r_s (third-down), and intermediate region's inverted power-law index n (bottom-most) resulting from the minimizations of the generalized RSS χ_{cosmo}^2 . The sub-panels of the second-to-last and last panels show the evolutions of r_s and n for optimizations utilizing χ_{ideal}^2 . Each scatter point represents a single snapshot in the simulation data sets, utilizing ρ_{R16} (brown), $\rho_{\text{R17-F24}}$ (purple), ρ_{Y23} (cyan), and ρ_{T24} (pink), as priors. All quantities are scaled as described in Section III C.

tailed analysis of which are discussed in Appendix D), our profile successfully provides good representations for the density and velocity dispersion structures. Note that this is only with the use of χ_{cosmo}^2 , and optimizations employing χ_{ideal}^2 produce more limited results. To quantify and compare the goodness of fit between density profiles throughout the different halos' developments, we investi-

gate the evolutions of the reduced RSSs shown in Figure 5. We observe that at the earlier times $t \lesssim 0.05 t_{\text{col}}$, the Read and the Robertson-Fischer profiles appear as the preferred prior for the density structures. This earlier epoch represents the initial thermalization of the halo core when the isothermal-core configuration is not yet established. Afterward, our density profile is significantly favored.

At the latest epochs, when the halos are on the onset of the gravothermal catastrophe and the LFMP limit begins to fail resulting in the invalidity of the self-similar solution, none of the profiles perform well. Nevertheless, even in this regime, our profile still provides the best fitting prior. Interestingly, we observe a particular phenomenon happening only with the optimizations of χ_{ideal}^2 utilizing our profile. The goodness of fit in these cases appears to have a strong correlation with the halo's epoch of evolution. This is not well understood, but we suspect that such a correlation may be the result of the particle fraction within the core enforcing a limit on the goodness of fit. Another possibility is that the correlation is related to some varying characteristics of the halo outer regions, the regression of which dominates the optimization of χ_{ideal}^2 . The goodness of fit resulting from χ_{cosmo}^2 , on the other hand, when either our profile or another is used, appears to be more stable, despite the general evolution characteristics remaining similar to the χ_{ideal}^2 cases.

Figure 6 visualizes the evolutions of the regressed parameters ρ_c , r_c , r_s , and n for all density profile priors. The evolution of n is excluded for the Read profile (where the intermediate region's power-law index always takes the value of $n = 1$). We choose to mainly display the results of optimizing χ_{cosmo}^2 as it typically provides better representations of the halo inner regions. The parameter evolutions emerging from both RSS choices are closely related, with significant differences occurring only in the Robertson-Fischer and the Yang profiles with the evolutions of r_s and n , where different evolution tracks appear when different RSSs are employed. Supplementary sub-panels are displayed to highlight these differences.

Generally, we observe the consistency across different halos within each profile family. The exception to this is with the evolution of the scale radius r_s in the Yang profile, where different halos evolve on different paths. This is reflected in the parameter evolution of both χ_{cosmo}^2 and χ_{ideal}^2 optimizations. The evolution of r_s in the Robertson-Fischer profile when χ_{ideal}^2 is optimized also shows the same characteristics, albeit to a lesser extent. We theorize that for the Yang profile (and possibly also for the Robertson-Fischer profile), r_s serves only as a nuisance parameter and is inadequate to represent the boundary between the intermediate region and the halo edge, hinting at the instability of the regressions utilizing the Yang profile.

All density profiles exhibit expected behaviors in the gravothermal collapse, namely having the core density approach infinity and the core radius vanish at later times. Except for in the Read profile, the regressed

core densities also closely match the values directly approximated from simulation data (obtained via the algorithm in Appendix B). Interestingly, we observe delays in the points of maximum core radius $t_{\text{max}(r_c)}$ in all profiles compared to the epoch of core density minimization $t_{\text{min}(\rho_c)}$. The exact moments of core density minimization and core radius maximization vary between prior choices; nevertheless, the typical delay is approximately $t_{\text{max}(r_c)} - t_{\text{min}(\rho_c)} \sim 0.06 t_{\text{col}}$. This is not well understood, as conventionally it is expected that the minimization of the core density and the maximization of the core radius happen simultaneously. Further investigation is needed.

All density profiles also exhibit convergences of the scale radius r_s and the intermediate region's inverted power-law index n to the values in the NFW configuration as $t \rightarrow 0$. This occurs strongly in the Robertson-Fischer profile but is weaker in the Yang and our profiles. In the evolutions of n , we also observe the evidence for self-similarity behaviors in the different halos, namely the stability of n after the initial thermalization phase, especially with our profile and the Yang profile. For the Robertson-Fischer profile, n is stable when χ_{ideal}^2 is used (i.e. when the fitting of the outer regions is prioritized) but fails when χ_{cosmo}^2 is utilized. This is most likely due to the strong influence of the halo outer regions on the characteristics of the inner regions in the Robertson-Fischer functional form (Figure 1), inferring a necessary sacrifice of the goodness of fit in either the halo core or its edge. Finally and interestingly, in our profile, the values of r_s also appear to plateau when χ_{ideal}^2 is used. This, along with the stability of n , hints at the non-involvement of the halo outer regions in the gravothermal collapse (theorized in [22, 23]) in addition to the self-similarity in the core.

Concerning observables such as the maximum circular velocity $V_{c,\text{max}}$ and radius $r_{V_{c,\text{max}}}$, although not explicitly shown, similar comparisons to those detailed in Appendix E using the fitting results of the different profiles rather than empirical formulae are performed. We observe strong deviations between the simulation data and the calculated values using the Read and the Robertson-Fischer profiles' regressions. For the Yang profile, the deviations are significantly smaller, only of the order of a few percentages. For our profile, even smaller deviations are observed with the calculated values matching simulation data almost perfectly. Appendix E presents the comparison using empirical evolutions of parameters, which is more convenient but results in slightly larger deviations.

IV. CONCLUSIONS AND DISCUSSIONS

In this work, we introduce a novel density profile for DM halos with self-interactions (Equation 11) that not only follows the flat-core configuration but also closely approximates the condition of isothermal cores. We believe that this profile provides a good representation of

DM halos in SIDM models. We show that

1. Analytically, halos with structure following our density profile possess close-to-flat velocity dispersions extending to a few of the characteristic core radii (i.e. the typical size of the flat-core region). This results in a high agreement with the isothermal-core configuration seen in the analytical self-similar solutions presented in [22, 23].
2. The density structure regressions performed with our density profile result in high levels of stability and the best density profile fits to various simulation data, regardless of the optimization criterion choice.
3. The reconstructed velocity dispersions resulting from the density structure fits based on our profile, as well as the inferred maximum circular velocities and radii, match closely to simulation data, while other density profiles fail to approximate the isothermal-core configuration, and their estimations of observables deviate significantly from simulations.

Except for the earliest epoch of the core formation phase and far into the deep core collapse regime, our profile works with high levels of agreement with simulation data.

As a result of being a good representation of DM halos in the self-similar scenarios, our profile can potentially be used to reduce the need for SIDM simulations with VICS models or can serve as an additional benchmark when comparisons between VICS and more complicated models are needed. This can be achieved with the empirical formulae detailed in Appendix E. Additionally, with the high level of representation of simulation data, the fits using our profile may reveal additional hidden structure evolution characteristics, such as the aforementioned delays in the maximization of core radius and minimization of core density. The resulting values for the intermediate region's inverted power-law indices n and the scale radii r_s can also be used to probe the self-similarity behaviors in more complicated SIDM models. With how well the profile performs in approximating the isothermal-core configuration, it can possibly further reveal characteristics of the analytical self-similar solution. Finally, initial conditions can potentially be constructed and generated from our density profile for simulations in the deep core collapse regime, reducing the need for evolving the halos at earlier epochs.

ACKNOWLEDGMENTS

We thank Philip Harris for useful discussions.

-
- [1] G. R. Blumenthal, S. M. Faber, J. R. Primack, and M. J. Rees, Formation of galaxies and large-scale structure with cold dark matter., *Nature* **311**, 517 (1984).
 - [2] M. Davis, G. Efstathiou, C. S. Frenk, and S. D. M. White, The evolution of large-scale structure in a universe dominated by cold dark matter, *ApJ* **292**, 371 (1985).
 - [3] J. S. Bullock and M. Boylan-Kolchin, Small-Scale Challenges to the Λ CDM Paradigm, *ARA&A* **55**, 343 (2017), arXiv:1707.04256 [astro-ph.CO].
 - [4] L. V. Sales, A. Wetzel, and A. Fattahi, Baryonic solutions and challenges for cosmological models of dwarf galaxies, *Nature Astronomy* **6**, 897 (2022), arXiv:2206.05295 [astro-ph.GA].
 - [5] R. A. Flores and J. R. Primack, Observational and Theoretical Constraints on Singular Dark Matter Halos, *ApJ* **427**, L1 (1994), arXiv:astro-ph/9402004 [astro-ph].
 - [6] B. Moore, Evidence against dissipation-less dark matter from observations of galaxy haloes, *Nature* **370**, 629 (1994).
 - [7] M. Boylan-Kolchin, J. S. Bullock, and M. Kaplinghat, Too big to fail? The puzzling darkness of massive Milky Way subhaloes, *MNRAS* **415**, L40 (2011), arXiv:1103.0007 [astro-ph.CO].
 - [8] K. A. Oman, J. F. Navarro, A. Fattahi, C. S. Frenk, T. Sawala, S. D. M. White, R. Bower, R. A. Crain, M. Furlong, M. Schaller, J. Schaye, and T. Theuns, The unexpected diversity of dwarf galaxy rotation curves, *MNRAS* **452**, 3650 (2015), arXiv:1504.01437 [astro-ph.GA].
 - [9] M. Kaplinghat, M. Valli, and H.-B. Yu, Too big to fail in light of Gaia, *MNRAS* **490**, 231 (2019), arXiv:1904.04939 [astro-ph.GA].
 - [10] L. Ackerman, M. R. Buckley, S. M. Carroll, and M. Kamionkowski, Dark matter and dark radiation, *Phys. Rev. D* **79**, 023519 (2009), arXiv:0810.5126 [hep-ph].
 - [11] N. Arkani-Hamed, D. P. Finkbeiner, T. R. Slatyer, and N. Weiner, A theory of dark matter, *Phys. Rev. D* **79**, 015014 (2009), arXiv:0810.0713 [hep-ph].
 - [12] F.-Y. Cyr-Racine and K. Sigurdson, Cosmology of atomic dark matter, *Phys. Rev. D* **87**, 103515 (2013), arXiv:1209.5752 [astro-ph.CO].
 - [13] S. Tulin and H.-B. Yu, Dark matter self-interactions and small scale structure, *Phys. Rep.* **730**, 1 (2018), arXiv:1705.02358 [hep-ph].
 - [14] In most cases, DM self-interactions are considered elastic for simplicity and will be the main focus of this paper, although inelastic DM self-interactions raised some attention recently [e.g. 38, 41, 43–45].
 - [15] M. Vogelsberger, J. Zavala, and A. Loeb, Subhaloes in self-interacting galactic dark matter haloes, *MNRAS* **423**, 3740 (2012), arXiv:1201.5892 [astro-ph.CO].
 - [16] M. Rocha, A. H. G. Peter, J. S. Bullock, M. Kaplinghat, S. Garrison-Kimmel, J. Oñorbe, and L. A. Moustakas, Cosmological simulations with self-interacting dark matter - I. Constant-density cores and substructure, *MNRAS* **430**, 81 (2013), arXiv:1208.3025 [astro-ph.CO].
 - [17] O. D. Elbert, J. S. Bullock, S. Garrison-Kimmel, M. Rocha, J. Oñorbe, and A. H. G. Peter, Core formation in dwarf haloes with self-interacting dark mat-

- ter: no fine-tuning necessary, *MNRAS* **453**, 29 (2015), arXiv:1412.1477 [astro-ph.GA].
- [18] F. Jiang, A. Benson, P. F. Hopkins, O. Slone, M. Lisanti, M. Kaplinghat, A. H. G. Peter, Z. C. Zeng, X. Du, S. Yang, and X. Shen, A semi-analytic study of self-interacting dark-matter haloes with baryons, *MNRAS* **521**, 4630 (2023), arXiv:2206.12425 [astro-ph.CO].
- [19] D. Gilman, Y.-M. Zhong, and J. Bovy, Constraining resonant dark matter self-interactions with strong gravitational lenses, *Phys. Rev. D* **107**, 103008 (2023), arXiv:2207.13111 [astro-ph.CO].
- [20] A. Burkert, The Structure and Evolution of Weakly Self-interacting Cold Dark Matter Halos, *ApJ* **534**, L143 (2000), arXiv:astro-ph/0002409 [astro-ph].
- [21] C. S. Kochanek and M. White, A Quantitative Study of Interacting Dark Matter in Halos, *ApJ* **543**, 514 (2000), arXiv:astro-ph/0003483 [astro-ph].
- [22] S. Balberg, S. L. Shapiro, and S. Inagaki, Self-Interacting Dark Matter Halos and the Gravothermal Catastrophe, *ApJ* **568**, 475 (2002), arXiv:astro-ph/0110561 [astro-ph].
- [23] D. Lynden-Bell and P. P. Eggleton, On the consequences of the gravothermal catastrophe, *MNRAS* **191**, 483 (1980).
- [24] Unitl reaching the short-mean-free-path regime when heat conduction is only effective at the surface of the core.
- [25] J. F. Navarro, C. S. Frenk, and S. D. M. White, A Universal Density Profile from Hierarchical Clustering, *ApJ* **490**, 493 (1997), arXiv:astro-ph/9611107 [astro-ph].
- [26] P. Colín, V. Avila-Reese, O. Valenzuela, and C. Firmani, Structure and Subhalo Population of Halos in a Self-interacting Dark Matter Cosmology, *ApJ* **581**, 777 (2002), arXiv:astro-ph/0205322 [astro-ph].
- [27] S. Yang, X. Du, Z. C. Zeng, A. Benson, F. Jiang, E. O. Nadler, and A. H. G. Peter, Gravothermal Solutions of SIDM Halos: Mapping from Constant to Velocity-dependent Cross Section, *ApJ* **946**, 47 (2023), arXiv:2205.02957 [astro-ph.CO].
- [28] J. I. Read, O. Agertz, and M. L. M. Collins, Dark matter cores all the way down, *MNRAS* **459**, 2573 (2016), arXiv:1508.04143 [astro-ph.GA].
- [29] A. Robertson, R. Massey, and V. Eke, What does the Bullet Cluster tell us about self-interacting dark matter?, *MNRAS* **465**, 569 (2017), arXiv:1605.04307 [astro-ph.CO].
- [30] M. S. Fischer, L. Kasselman, M. Brüggen, K. Dolag, F. Kahlhoefer, A. Ragagnin, A. Robertson, and K. Schmidt-Hoberg, Cosmological and idealized simulations of dark matter haloes with velocity-dependent, rare and frequent self-interactions, *MNRAS* **529**, 2327 (2024), arXiv:2310.07750 [astro-ph.CO].
- [31] D. Yang, E. O. Nadler, H.-B. Yu, and Y.-M. Zhong, A parametric model for self-interacting dark matter halos, *J. Cosmol. Astropart. Phys.* **2024**, 032 (2024), arXiv:2305.16176 [astro-ph.CO].
- [32] M. Kaplinghat, S. Tulin, and H.-B. Yu, Dark Matter Halos as Particle Colliders: Unified Solution to Small-Scale Structure Puzzles from Dwarfs to Clusters, *Phys. Rev. Lett.* **116**, 041302 (2016), arXiv:1508.03339 [astro-ph.CO].
- [33] V. Tran, D. Gilman, M. Vogelsberger, X. Shen, S. O'Neil, and X. Zhang, Gravothermal catastrophe in resonant self-interacting dark matter models, *Phys. Rev. D* **110**, 043048 (2024), arXiv:2405.02388 [astro-ph.GA].
- [34] V. Tran, D. Gilman, M. Vogelsberger, X. Shen, and S. O'Neil, Structure evolution of low-mass dark matter halos in resonant self-interacting dark matter models, in preparation.
- [35] C. Mace, Z. Carton Zeng, A. H. G. Peter, X. Du, S. Yang, A. Benson, and M. Vogelsberger, Convergence Tests of Self-Interacting Dark Matter Simulations, arXiv e-prints , arXiv:2402.01604 (2024), arXiv:2402.01604 [astro-ph.GA].
- [36] I. Palubski, O. Slone, M. Kaplinghat, M. Lisanti, and F. Jiang, Numerical Challenges in Modeling Gravothermal Collapse in Self-Interacting Dark Matter Halos, arXiv e-prints , arXiv:2402.12452 (2024), arXiv:2402.12452 [astro-ph.CO].
- [37] X. Shen, P. F. Hopkins, L. Necib, F. Jiang, M. Boylan-Kolchin, and A. Wetzel, Dissipative Dark Matter on FIRE: II. Observational signatures and constraints from local dwarf galaxies, arXiv e-prints , arXiv:2206.05327 (2022), arXiv:2206.05327 [astro-ph.GA].
- [38] R. Essig, S. D. McDermott, H.-B. Yu, and Y.-M. Zhong, Constraining Dissipative Dark Matter Self-Interactions, *Phys. Rev. Lett.* **123**, 121102 (2019), arXiv:1809.01144 [hep-ph].
- [39] Y.-M. Zhong, D. Yang, and H.-B. Yu, The impact of baryonic potentials on the gravothermal evolution of self-interacting dark matter haloes, *MNRAS* **526**, 758 (2023), arXiv:2306.08028 [astro-ph.CO].
- [40] J. Koda and P. R. Shapiro, Gravothermal collapse of isolated self-interacting dark matter haloes: N-body simulation versus the fluid model, *MNRAS* **415**, 1125 (2011), arXiv:1101.3097 [astro-ph.CO].
- [41] X. Shen, P. F. Hopkins, L. Necib, F. Jiang, M. Boylan-Kolchin, and A. Wetzel, Dissipative dark matter on FIRE - I. Structural and kinematic properties of dwarf galaxies, *MNRAS* **506**, 4421 (2021), arXiv:2102.09580 [astro-ph.GA].
- [42] D. Yang and H.-B. Yu, Gravothermal evolution of dark matter halos with differential elastic scattering, *J. Cosmol. Astropart. Phys.* **2022**, 077 (2022), arXiv:2205.03392 [astro-ph.CO].
- [43] M. Vogelsberger, J. Zavala, K. Schutz, and T. R. Slatyer, Evaporating the Milky Way halo and its satellites with inelastic self-interacting dark matter, *MNRAS* **484**, 5437 (2019), arXiv:1805.03203 [astro-ph.GA].
- [44] X. Shen, P. Hopkins, L. Necib, F. Jiang, M. Boylan-Kolchin, and A. Wetzel, Dissipative Dark Matter on FIRE: Structural and kinematic properties of dwarf galaxies and observational constraints, in *American Astronomical Society Meeting #240*, American Astronomical Society Meeting Abstracts, Vol. 240 (2022) p. 347.06.
- [45] S. O'Neil, M. Vogelsberger, S. Heeba, K. Schutz, J. C. Rose, P. Torrey, J. Borrow, R. Low, R. Adhikari, M. V. Medvedev, T. R. Slatyer, and J. Zavala, Endothermic self-interacting dark matter in Milky Way-like dark matter haloes, *MNRAS* **524**, 288 (2023), arXiv:2210.16328 [astro-ph.GA].
- [46] G. R. Blumenthal, S. M. Faber, R. Flores, and J. R. Primack, Contraction of Dark Matter Galactic Halos Due to Baryonic Infall, *ApJ* **301**, 27 (1986).
- [47] O. Y. Gnedin, A. V. Kravtsov, A. A. Klypin, and D. Nagai, Response of Dark Matter Halos to Condensation of Baryons: Cosmological Simulations and Improved Adiabatic Contraction Model, *ApJ* **616**, 16 (2004), arXiv:astro-ph/0406247 [astro-ph].

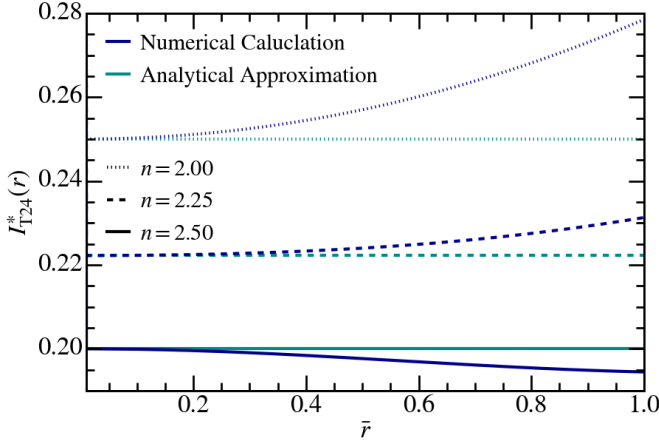


FIG. 7. The core isothermal K-G ratios resulting from the trial density profile $\rho_{T24}^*(r)$ (Equation 10). Three choices of intermediate region’s inverted power-law indices $n = 2, 2.25, 2.5$ are shown in dotted, dashed, and solid lines. The blue lines show the numerical calculations following Equation 9, while the cyan lines display the analytical approximation derived from Equation A11.

Appendix A: Analytical Calculation of the Core Velocity Dispersion via the Isothermal K-G Ratio

To inspect the core isothermal K-G ratio (Equation 9) of our density profile, we first separate $\bar{\rho}_{T24}(r)$ into

$$g(\bar{r}) = \left(\frac{\tanh \bar{r}}{\bar{r}} \right)^n, \quad (\text{A1})$$

$$h(\bar{r}) = \frac{1}{(1 + (\lambda \bar{r})^\gamma)^{\frac{3-n}{\gamma}}}, \quad (\text{A2})$$

with $\lambda = r_c/r_s$. Here, $g(\bar{r})$ and $h(\bar{r})$ represent the approximate density profile of the halo inner part and the modifier for the halo outer edge. Taking the $\bar{r} \ll 1$ approximations, specifically

$$\frac{\tanh \bar{r}}{\bar{r}} = 1 + \mathcal{O}(\bar{r}^2), \quad (\text{A3})$$

$$\text{sech}^2 \bar{r} \approx 1 + \mathcal{O}(\bar{r}^2), \quad (\text{A4})$$

$$\frac{\tanh \bar{r}}{\bar{r}} - \text{sech}^2 \bar{r} \approx \frac{2}{3}\bar{r}^2 + \mathcal{O}(\bar{r}^4), \quad (\text{A5})$$

$$1 + (\lambda \bar{r})^\gamma \approx 1 + \mathcal{O}(\bar{r}^\gamma), \quad (\text{A6})$$

we obtain the first and second derivatives

$$g'(\bar{r}) = -\frac{2n}{3}\bar{r} + \mathcal{O}(\bar{r}^3), \quad (\text{A7})$$

$$g''(\bar{r}) = -2n + \frac{4n^2}{9}\bar{r}^2 + \frac{2n}{3} + \frac{2n}{3} + \mathcal{O}(\bar{r}^2), \quad (\text{A8})$$

$$h'(\bar{r}) = -(3-n) \frac{(\lambda \bar{r})^\gamma}{\bar{r}} + \mathcal{O}(\bar{r}^{2\gamma-1}), \quad (\text{A9})$$

$$h''(\bar{r}) = -(3-n)(\gamma-1) \frac{(\lambda \bar{r})^\gamma}{\bar{r}^2} + \mathcal{O}(\bar{r}^{2\gamma-2}). \quad (\text{A10})$$

Considering only the simplified trial density profile, $\rho(\bar{r}) = g(\bar{r})$, the resulting core isothermal K-G ratio takes the form of

$$I_{c,T24}^*(r) = \frac{1}{2n} + \mathcal{O}(\bar{r}^2), \quad (\text{A11})$$

which is independent of radius (to the order of \bar{r}^2). The comparisons of this prediction with the numerical results following Equation 9 are shown in Figure 7. When the outer edge modifier $h(\bar{r})$ is included, the core isothermal K-G ratio would follow

$$I_{c,T24}(r) \approx \left(2n + (3-n)(\gamma+1) \frac{(\lambda \bar{r})^\gamma}{\bar{r}^2} \right)^{-1}. \quad (\text{A12})$$

Here, the extra term $-(3-n)^2(\lambda \bar{r})^{2\gamma}/\bar{r}^2$ inside the parentheses has been ignored. It is clear from Equation A12 that unless $\gamma \geq 2$, $(\lambda \bar{r})^\gamma/\bar{r}^2 \rightarrow \infty$ and $I_{c,T24} \rightarrow 0$. In fact, $\gamma = 2$ represents a special case with

$$I_{c,T24}(r) = \frac{1}{2n + 3(3-n)\lambda^2} + \mathcal{O}(\bar{r}^2), \quad (\text{A13})$$

while, otherwise,

$$I_{c,T24}(r) = \frac{1}{2n + (3-n)(\gamma+1)\lambda^2 \bar{r}^{\gamma-2}} + \mathcal{O}(\bar{r}^2). \quad (\text{A14})$$

The first case provides a near-optimal situation, with $I_{c,T24}(r)$ becoming practically independent of \bar{r} similar to in the idealistic configuration. In most cases, $\lambda \ll 1$, resulting in the core isothermal K-G ratio reverting to the form displayed by Equation A11.

Appendix B: Direct Approximation of Halo Core Density

The approximated core density mentioned in Section IIIB is obtained via the following algorithm.

1. Start from the “zero count” (the number of particles within the smallest radial bin edge) as the accumulated core count.
2. Calculate the average core density ρ_{core} and uncertainty $\sigma_{\rho_{\text{core}}}$ from the accumulated core count, assuming Poisson statistics.
3. Calculate the enveloping shell average density ρ_{shell} and uncertainty $\sigma_{\rho_{\text{shell}}}$, again assuming Poisson statistics.
4. If the accumulated core count $< N_{\text{min}}$, taken to be $N_{\text{min}} = 2500$, or $|\rho_{\text{core}} - \rho_{\text{shell}}| < \sqrt{\sigma_{\rho_{\text{core}}}^2 + \sigma_{\rho_{\text{shell}}}^2}$, add the shell count to the accumulated core count, and repeat from step 2.
5. Else, take ρ_{core} and $\sigma_{\rho_{\text{core}}}$ as the approximation for the core density and its uncertainty.

The criteria in step 4 are set empirically, and looser (or stricter) boundaries can be chosen depending on the simulation settings and statistical requirements.

Appendix C: Simulations Configuration of the Larger data set

$\log M_{200}$ [M_{\odot}]	c	r_s [kpc]	$\log \rho_s$ [$M_{\odot} \text{ kpc}^{-3}$]	σ/m [$\text{cm}^2 \text{ g}^{-1}$]
6.5	22.63	0.14	7.65	21.84
7	21.21	0.21	7.57	24.94
7	21.21	0.21	7.57	19.81
7.5	19.81	0.34	7.50	43.54
7.5	19.81	0.34	7.50	19.76
8	18.42	0.53	7.42	28.07
8	18.42	0.53	7.42	21.94
8.5	17.05	0.84	7.33	14.62
8.5	17.05	0.84	7.33	18.60
9	15.69	1.35	7.24	8.87
9	15.69	1.35	7.24	13.09
9.5	14.37	2.16	7.14	8.23

TABLE II. Simulations configuration of the larger data set [34]. (1) M_{200} is the virial mass of the halo. (2) c is the halo concentration parameter. (4) ρ_s and (3) r_s are the scale density and radius of the NFW profile. (5) σ/m is the SIDM collisions' cross section per unit of mass.

Appendix D: Density Profile Fits at Different Evolution Epochs

Figure 8 presents the density profile fits and reconstructions of the velocity dispersions two snapshots taken from the simulation of the $10^{7.5} M_{\odot}$ halo evolved under the VICS of $\sigma/m = 43.54 \text{ cm}^2 \text{ g}^{-1}$ (i.e. the same simulation used for the fittings and reconstructions displayed in Figure 4). These two snapshots, presenting the halo at $t \simeq 0.02 t_{\text{col}}$ and $t \simeq 0.88 t_{\text{col}}$, represent the earliest epoch of the initial thermalization phase and a typical epoch at the deep core collapse regime's onset. Even at these extreme snapshots, our density profile remains capable of producing good representations for the halo's density and velocity dispersion structures, especially in the case of optimizing χ_{cosmo}^2 . In the earlier snapshot, however, other profile choices appear to perform better in approximating the halo's density configuration. This is evident in the fluctuation of the density profile residuals, with our profile performing significantly worse at regressing the halo outer regions. Nevertheless, a closer inspection of the reconstructed velocity dispersions reveals significant deviations from simulation data when other profile choices are utilized. Despite the sub-optimal representation of the density structure, our profile provides a much better velocity dispersion reconstruction. In the later snapshots, all profile choices fail to closely represent the simulation data. Nonetheless, our profile still produces a decent approximation of the density, as well as a sur-

prisingly close representation of the velocity dispersions, albeit with the deviation increases to $\simeq 2\%$.

Appendix E: Empirical Evolutions of Parameters in the Self-similar Solution

Using the fitting results of Section III C (the tabular form of which is presented in Table III), we arrive at a general set of empirical equations describing the evolutions of $\rho_{c,T24}$, $r_{c,T24}$, $r_{s,T24}$, and n_{T24} . These equations can serve as good references when comparisons between simple VICS models and more complicated SIDM models are needed, especially in the context of idealized isolated halos.

To most accurately represent the configurations of halos, we use the values of $\rho_{c,T24}$, $r_{c,T24}$, and n_{T24} regressed from the optimization of χ_{cosmo}^2 , while values of $r_{s,T24}$ are taken from the fits using χ_{ideal}^2 . This is because χ_{cosmo}^2 produces closer approximations of the halo core's structure, and the resulting evolution tracks from different halos appear more consistent with each other. Nevertheless, χ_{ideal}^2 provides better representations for the halo outer regions, where $r_{s,T24}$ is most concerned. For simplicity, we construct the empirical equations only out of polynomials and square/cube roots. Constraints in the initial conditions are also enforced to map the density profile back to the NFW configuration. These are $\rho_{c,\tilde{t}=0} \rightarrow \infty$, $r_{c,\tilde{t}=0} = 0$, $r_{s,\tilde{t}=0} = r_{s,\text{NFW}}$, and $n_{\tilde{t}=0} = 1$. More idealistically, the condition of $\rho_{c,\tilde{t}=0} r_{c,\tilde{t}=0} = \rho_{s,\text{NFW}} r_{s,\text{NFW}}$ should also be satisfied. However, we find that this is a difficult constraint to implement and, thus, ignore it. The resulting empirical fits then follow

$$\frac{\rho_{c,T24}}{\rho_{s,\text{NFW}}} = \frac{1}{\tilde{t}(1-\tilde{t})} \left(-4.221 \tilde{t} + 3.572 \tilde{t}^2 - 2.312 \tilde{t}^3 + 3.898 \sqrt{\tilde{t}} - 0.908 \sqrt[3]{\tilde{t}} \right)^{-1}, \quad (\text{E1})$$

$$\frac{r_{c,T24}}{r_{s,\text{NFW}}} = -3.110 \tilde{t} + 2.066 \tilde{t}^2 - 1.149 \tilde{t}^3 + 2.229 \sqrt{\tilde{t}} - 0.044 \sqrt[3]{\tilde{t}}, \quad (\text{E2})$$

$$\frac{r_{s,T24}}{r_{s,\text{NFW}}} = 1 + 12.455 \tilde{t} - 8.785 \tilde{t}^2 + 0.556 \tilde{t}^3 - 8.364 \sqrt{\tilde{t}} + 14.706 \sqrt[3]{\tilde{t}}, \quad (\text{E3})$$

$$n_{T24} = 1 - 1.978 \tilde{t} + 2.417 \tilde{t}^2 - 1.293 \tilde{t}^3 - 3.550 \sqrt{\tilde{t}} + 5.745 \sqrt[3]{\tilde{t}}. \quad (\text{E4})$$

Here, $\tilde{t} = t/t_{\text{col}}$ is the scaled collapse time. In more complicated velocity-dependent cross section models, such as those with resonant cross sections, where the collapse

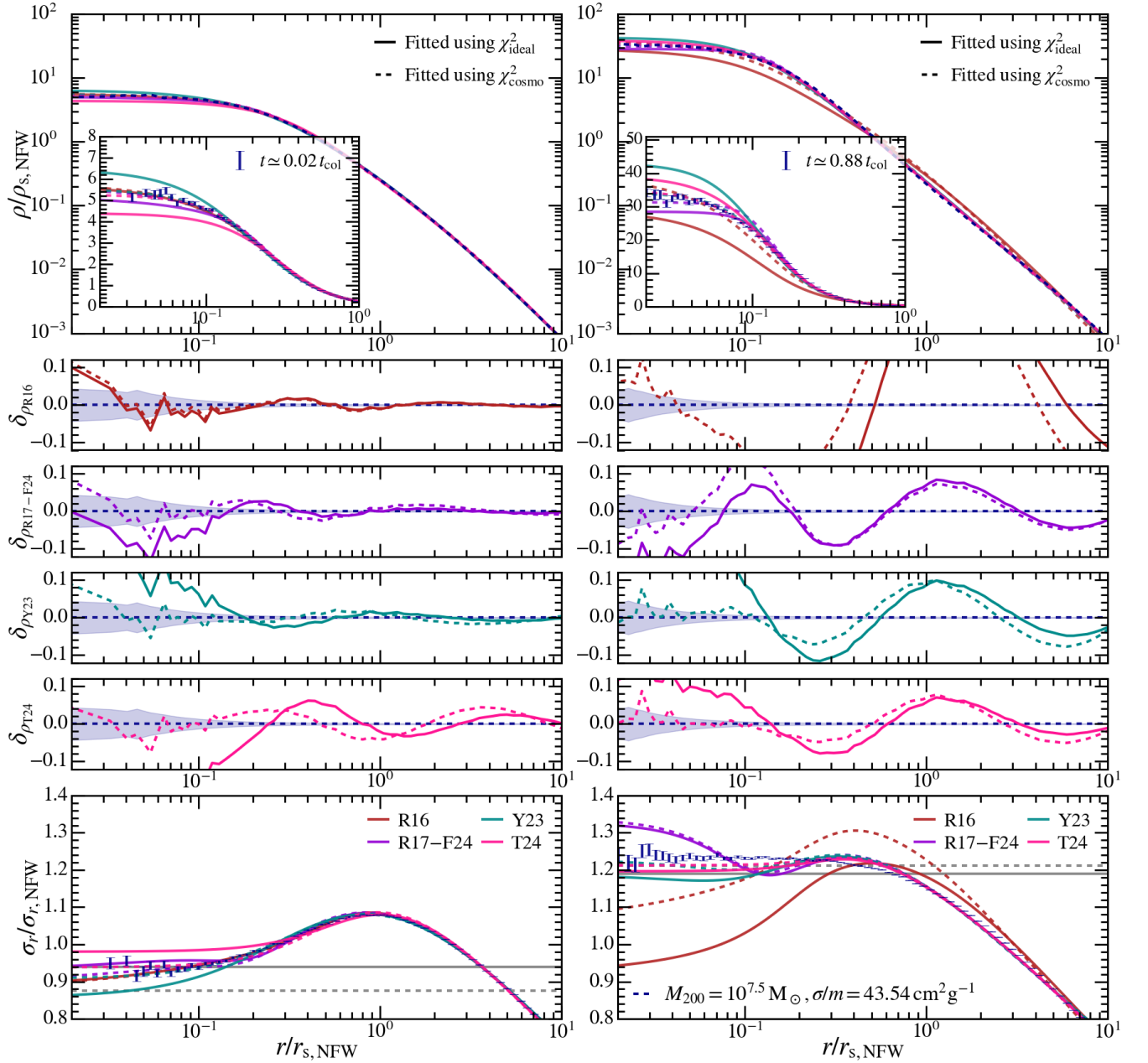


FIG. 8. The density profile fits and velocity dispersion profile reconstructions for the snapshots at $t \simeq 0.02 t_{\text{col}}$ (left) and $t \simeq 0.88 t_{\text{col}}$ (right) of the $10^{7.5} M_{\odot}$ halo evolved under the VICS of $\sigma/m = 43.54 \text{ cm}^2 \text{ g}^{-1}$. The panels are the same as shown in Figure 4.

time scales t_{col} vary over time, as a result of changing σ_{eff}/m , \hat{t} can be retrieved from $dt = t_{\text{col}}(\hat{t}) d\hat{t}$ as detailed in [33]. Here, we calculate t_{col} with the value of $C \simeq 0.85$.

From the empirical evolutions of $\rho_{c,T24}$, $r_{c,T24}$, $r_{s,T24}$, and n_{T24} , the evolution tracks of the core velocity dispersion σ_c , the maximum circular velocity $V_{c,\text{max}}$, and the maximum circular velocity radius $r_{V_{c,\text{max}}}$ can be obtained (as shown in Figure 9). Up until $t \simeq 0.8 t_{\text{col}}$, the simulation inferred values are almost exactly matched by our approximations. However, in the interval of $0.8 t_{\text{col}} \lesssim t \lesssim 0.9 t_{\text{col}}$, deviations of the order of $\sim 2 - 5\%$

in σ_c and $V_{c,\text{max}}$ start to appear. Beyond $t \simeq 0.9 t_{\text{col}}$, our simulation datasets are unavailable, as the halos enter the deep core collapse regime. Nevertheless, the evolutions extrapolated by the empirical tracks are most likely unrealistic. Modifications of the model are possibly required in this regime.

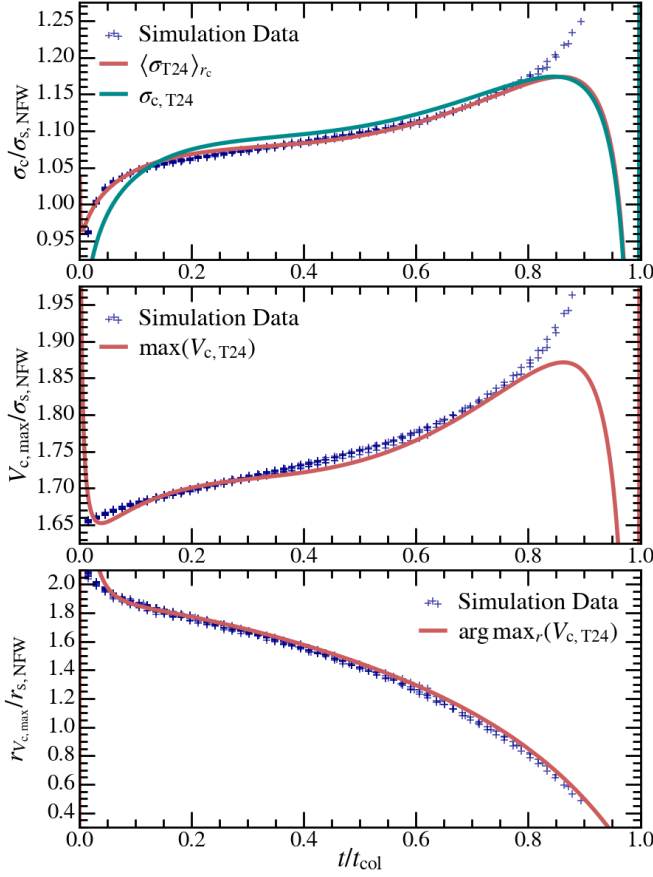


FIG. 9. The comparisons between the empirical evolution tracks (red lines) and the simulation approximations (blue scatters) of the core velocity dispersion σ_c (top), maximum circular velocity $V_{c,\max}$ (center), and maximum circular velocity radius $r_{V_{c,\max}}$ (bottom). The empirical tracks are calculated from profiles with parameter evolutions following Equation E1, E2, E3, and E4. For the core velocity dispersion, two empirical tracks are presented, with $\sigma_{c,T24}$ (cyan) calculated from Equation 12 and $\langle\sigma_{T24}\rangle_{r_c}$ (red) taken as the average velocity dispersions within r_c . The simulation approximations σ_{core} are also calculated similar to $\langle\sigma_{T24}\rangle_{r_c}$ using the simulation data. The exact radii at which the average core velocity dispersions are calculated are not important, as long as they are sufficiently small to represent the isothermal core and sufficiently large to ensure statistical stability.

t	$\rho_{c,T24}$	$r_{c,T24}$	$r_{s,T24}$	n_{T24}
[Gyr]	$[\rho_{s,\text{NFW}}]$	$[r_{s,\text{NFW}}]$	$[r_{s,\text{NFW}}]$	
$M_{200} = 10^{6.5} M_{\odot}, \sigma/m = 21.84 \text{ cm}^2 \text{ g}^{-1}$				
1.92	5.22	0.22	4.14	1.96
3.84	3.76	0.29	4.76	2.14
5.76	3.21	0.33	5.24	2.23
7.68	2.96	0.35	5.67	2.28
9.60	2.76	0.38	6.06	2.33
11.52	2.65	0.39	6.42	2.36
13.44	2.57	0.40	6.74	2.39

15.36	2.55	0.41	7.02	2.40
17.28	2.49	0.42	7.29	2.42
19.20	2.50	0.42	7.45	2.43
21.12	2.48	0.42	7.71	2.45
23.04	2.51	0.42	7.89	2.44
24.96	2.50	0.42	8.10	2.46
$M_{200} = 10^7 M_{\odot}, \sigma/m = 24.94 \text{ cm}^2 \text{ g}^{-1}$				
1.38	5.27	0.21	3.99	1.95
2.76	3.83	0.28	4.58	2.12
4.14	3.25	0.33	5.05	2.22
5.52	2.99	0.35	5.49	2.27
6.90	2.78	0.37	5.86	2.32
8.28	2.67	0.39	6.22	2.35
9.66	2.63	0.39	6.51	2.37
11.04	2.55	0.41	6.82	2.40
12.42	2.52	0.41	7.10	2.41
13.80	2.53	0.41	7.35	2.42
15.18	2.50	0.42	7.56	2.44
16.56	2.52	0.42	7.74	2.44
17.94	2.53	0.42	7.96	2.45
19.32	2.54	0.42	8.11	2.46
20.70	2.55	0.42	8.30	2.47
22.08	2.57	0.42	8.50	2.48
23.46	2.60	0.42	8.65	2.48
24.84	2.65	0.42	8.83	2.48
26.22	2.70	0.41	8.96	2.48
27.60	2.75	0.41	9.13	2.48
28.98	2.75	0.41	9.31	2.49
30.36	2.81	0.41	9.46	2.49
31.74	2.85	0.41	9.54	2.50
33.12	2.92	0.40	9.68	2.50
34.50	3.00	0.40	9.83	2.50
35.88	3.06	0.40	9.95	2.50
37.26	3.16	0.39	10.05	2.50
38.64	3.20	0.39	10.20	2.50
40.02	3.28	0.38	10.28	2.50
41.40	3.38	0.38	10.32	2.50
42.78	3.48	0.37	10.52	2.50
44.16	3.56	0.37	10.56	2.51
45.54	3.66	0.37	10.67	2.50
46.92	3.80	0.36	10.76	2.50
48.30	3.93	0.35	10.89	2.50
49.68	4.05	0.35	10.93	2.50
51.06	4.17	0.34	11.10	2.50
52.44	4.32	0.34	11.14	2.50
53.82	4.47	0.33	11.24	2.50
55.20	4.63	0.33	11.23	2.50
56.58	4.86	0.32	11.40	2.50
$M_{200} = 10^7 M_{\odot}, \sigma/m = 19.81 \text{ cm}^2 \text{ g}^{-1}$				
1.74	5.27	0.21	3.99	1.95

3.48	3.75	0.29	4.61	2.13	17.82	3.26	0.38	10.09	2.50
5.22	3.23	0.33	5.08	2.22	18.48	3.33	0.38	10.23	2.50
6.96	2.94	0.35	5.49	2.28	19.14	3.42	0.38	10.39	2.50
8.70	2.77	0.37	5.89	2.32	19.80	3.50	0.37	10.51	2.50
10.44	2.66	0.39	6.25	2.36	20.46	3.59	0.37	10.56	2.50
12.18	2.59	0.40	6.55	2.38	21.12	3.74	0.36	10.68	2.50
13.92	2.54	0.41	6.83	2.40	21.78	3.89	0.35	10.70	2.50
15.66	2.52	0.41	7.09	2.41	22.44	3.98	0.35	10.85	2.50
17.40	2.48	0.42	7.33	2.44	23.10	4.12	0.35	10.88	2.50
19.14	2.50	0.42	7.50	2.44	23.76	4.30	0.34	10.97	2.50
20.88	2.49	0.42	7.74	2.45	24.42	4.43	0.34	11.09	2.50
22.62	2.51	0.42	7.95	2.46	25.08	4.70	0.33	11.17	2.50
24.36	2.56	0.42	8.15	2.46	25.74	4.89	0.32	11.24	2.50
26.10	2.56	0.42	8.36	2.47	26.40	5.10	0.31	11.30	2.50
27.84	2.56	0.42	8.56	2.48	27.06	5.40	0.31	11.32	2.49
29.58	2.62	0.42	8.76	2.48	27.72	5.73	0.30	11.45	2.49
31.32	2.65	0.42	8.90	2.49	28.38	6.08	0.29	11.51	2.49
33.06	2.68	0.42	9.04	2.49	29.04	6.43	0.28	11.57	2.49
34.80	2.75	0.41	9.22	2.49	29.70	6.91	0.27	11.55	2.48
36.54	2.77	0.41	9.37	2.49	30.36	7.43	0.26	11.63	2.48
38.28	2.85	0.41	9.48	2.49	31.02	8.17	0.25	11.68	2.48
40.02	2.88	0.41	9.60	2.50	31.68	8.82	0.24	11.66	2.47
41.76	2.90	0.41	9.77	2.51	32.34	9.58	0.23	11.66	2.47
<hr/> $M_{200} = 10^{7.5} M_{\odot}, \sigma/m = 43.54 \text{ cm}^2 \text{ g}^{-1}$ <hr/>					33.00	10.56	0.22	11.73	2.47
0.66	5.27	0.21	3.91	1.95	33.66	11.45	0.22	11.77	2.47
1.32	3.76	0.29	4.51	2.13	34.32	12.82	0.20	11.84	2.46
1.98	3.25	0.33	4.99	2.21	34.98	14.19	0.19	11.80	2.46
2.64	2.99	0.35	5.41	2.27	35.64	16.12	0.18	11.79	2.45
3.30	2.78	0.37	5.79	2.32	36.30	18.89	0.17	11.75	2.45
3.96	2.71	0.38	6.09	2.34	36.96	22.20	0.16	11.73	2.44
4.62	2.59	0.40	6.39	2.38	37.62	26.82	0.14	11.61	2.44
5.28	2.55	0.41	6.72	2.40	38.28	34.96	0.13	11.50	2.43
5.94	2.54	0.41	7.00	2.41	<hr/> $M_{200} = 10^{7.5} M_{\odot}, \sigma/m = 19.76 \text{ cm}^2 \text{ g}^{-1}$ <hr/>				
6.60	2.53	0.41	7.20	2.42	1.44	5.28	0.21	3.90	1.95
7.26	2.51	0.42	7.46	2.44	2.88	3.76	0.29	4.50	2.13
7.92	2.53	0.42	7.63	2.45	4.32	3.21	0.33	4.97	2.22
8.58	2.51	0.42	7.91	2.46	5.76	2.92	0.36	5.42	2.28
9.24	2.55	0.42	8.13	2.46	7.20	2.76	0.37	5.78	2.32
9.90	2.59	0.42	8.35	2.46	8.64	2.66	0.39	6.12	2.35
10.56	2.65	0.41	8.52	2.46	10.08	2.61	0.40	6.44	2.37
11.22	2.62	0.42	8.68	2.48	11.52	2.54	0.41	6.70	2.40
11.88	2.67	0.42	8.86	2.48	12.96	2.51	0.41	7.01	2.41
12.54	2.70	0.42	9.06	2.49	14.40	2.53	0.41	7.23	2.42
13.20	2.78	0.41	9.24	2.49	15.84	2.51	0.42	7.48	2.43
13.86	2.81	0.41	9.40	2.49	17.28	2.51	0.42	7.71	2.44
14.52	2.84	0.41	9.52	2.50	18.72	2.49	0.42	7.93	2.46
15.18	2.94	0.40	9.66	2.49	20.16	2.51	0.42	8.07	2.46
15.84	2.98	0.40	9.82	2.50	21.60	2.54	0.42	8.28	2.47
16.50	3.05	0.40	9.92	2.50	23.04	2.57	0.42	8.50	2.47
17.16	3.14	0.39	10.05	2.50	24.48	2.61	0.42	8.65	2.47

25.92	2.59	0.42	8.85	2.49	45.63	41.81	0.12	11.47	2.42
27.36	2.67	0.42	9.01	2.49	$M_{200} = 10^8 M_{\odot}, \sigma/m = 28.07 \text{ cm}^2 \text{ g}^{-1}$				
28.80	2.66	0.42	9.23	2.50	0.85	5.31	0.21	3.82	1.94
30.24	2.75	0.41	9.36	2.49	1.70	3.84	0.28	4.40	2.11
31.68	2.80	0.41	9.43	2.49	2.55	3.30	0.32	4.86	2.20
33.12	2.83	0.41	9.70	2.50	3.40	2.96	0.35	5.29	2.27
34.56	2.90	0.41	9.76	2.50	4.25	2.81	0.37	5.65	2.31
36.00	2.97	0.40	9.85	2.50	5.10	2.67	0.39	6.00	2.35
37.44	3.04	0.40	10.02	2.50	5.95	2.60	0.40	6.32	2.38
38.88	3.11	0.39	10.14	2.50	6.80	2.57	0.40	6.62	2.39
40.32	3.20	0.39	10.22	2.50	7.65	2.53	0.41	6.89	2.42
41.76	3.27	0.39	10.31	2.50	8.50	2.53	0.41	7.16	2.42
43.20	3.36	0.38	10.40	2.50	9.35	2.53	0.42	7.42	2.43
$M_{200} = 10^{7.9} M_{\odot}, \sigma/m = 31.98 \text{ cm}^2 \text{ g}^{-1}$					10.20	2.53	0.42	7.67	2.45
2.34	3.25	0.33	4.92	2.21	11.05	2.53	0.42	7.89	2.46
3.51	2.87	0.36	5.56	2.30	11.90	2.55	0.42	8.12	2.46
4.68	2.74	0.38	6.09	2.33	12.75	2.58	0.42	8.32	2.47
5.85	2.58	0.40	6.57	2.39	13.60	2.62	0.42	8.54	2.47
7.02	2.56	0.41	7.02	2.41	14.45	2.64	0.42	8.76	2.48
8.19	2.54	0.41	7.37	2.43	15.30	2.68	0.42	8.85	2.48
9.36	2.51	0.42	7.81	2.45	16.15	2.73	0.41	9.02	2.48
10.53	2.51	0.43	8.08	2.47	17.00	2.75	0.41	9.17	2.49
11.70	2.60	0.42	8.37	2.47	17.85	2.79	0.41	9.35	2.50
12.87	2.64	0.42	8.57	2.47	18.70	2.87	0.41	9.45	2.49
14.04	2.69	0.41	8.73	2.48	19.55	2.93	0.40	9.62	2.50
15.21	2.73	0.41	8.96	2.49	20.40	3.01	0.40	9.69	2.50
16.38	2.79	0.41	9.16	2.50	21.25	3.08	0.39	9.82	2.50
18.72	2.98	0.40	9.56	2.50	22.10	3.14	0.39	9.99	2.50
19.89	3.09	0.39	9.78	2.50	22.95	3.22	0.39	10.10	2.50
21.06	3.19	0.39	9.99	2.51	23.80	3.32	0.38	10.19	2.50
22.23	3.32	0.38	10.21	2.51	24.65	3.39	0.38	10.30	2.50
23.40	3.50	0.37	10.40	2.50	25.50	3.53	0.37	10.45	2.50
24.57	3.68	0.36	10.57	2.50	26.35	3.65	0.37	10.60	2.50
25.74	3.79	0.36	10.77	2.51	27.20	3.71	0.36	10.65	2.51
26.91	4.10	0.35	10.90	2.50	28.05	3.87	0.36	10.79	2.50
28.08	4.30	0.34	11.03	2.50	28.90	3.98	0.35	10.92	2.51
29.25	4.65	0.33	11.12	2.50	29.75	4.19	0.34	10.91	2.50
30.42	4.96	0.32	11.30	2.50	30.60	4.33	0.34	11.06	2.50
31.59	5.38	0.31	11.35	2.49	31.45	4.50	0.33	11.19	2.50
32.76	5.90	0.29	11.39	2.49	32.30	4.75	0.32	11.27	2.50
33.93	6.51	0.28	11.46	2.48	33.15	4.95	0.32	11.31	2.50
35.10	7.08	0.27	11.59	2.48	34.00	5.26	0.31	11.43	2.49
36.27	7.90	0.26	11.57	2.48	34.85	5.43	0.31	11.50	2.50
37.44	8.81	0.24	11.68	2.47	35.70	5.80	0.30	11.53	2.49
38.61	9.80	0.23	11.73	2.47	36.55	6.04	0.29	11.61	2.49
39.78	11.39	0.22	11.82	2.47	37.40	6.41	0.28	11.68	2.49
40.95	13.28	0.20	11.83	2.46	38.25	6.80	0.27	11.75	2.49
42.12	16.26	0.18	11.84	2.45	39.10	7.15	0.27	11.76	2.49
43.29	20.39	0.16	11.76	2.45	39.95	7.69	0.26	11.75	2.48
44.46	27.37	0.14	11.70	2.44	40.80	8.21	0.25	11.87	2.48

41.65	8.85	0.24	11.94	2.48
42.50	9.74	0.23	11.98	2.47
43.35	10.48	0.22	11.99	2.47
44.20	11.65	0.21	11.98	2.47
45.05	12.94	0.20	12.03	2.46
45.90	14.73	0.19	12.00	2.46
46.75	16.79	0.18	12.02	2.45

$M_{200} = 10^8 M_{\odot}, \sigma/m = 21.97 \text{ cm}^2 \text{ g}^{-1}$

1.09	5.30	0.21	3.83	1.93
2.18	3.82	0.28	4.41	2.11
3.27	3.26	0.32	4.87	2.21
4.36	2.96	0.35	5.31	2.27
5.45	2.77	0.37	5.65	2.32
6.54	2.65	0.39	6.05	2.36
7.63	2.60	0.40	6.34	2.38
8.72	2.55	0.41	6.67	2.40
9.81	2.50	0.42	6.99	2.42
10.90	2.48	0.42	7.24	2.43
11.99	2.50	0.42	7.50	2.44
13.08	2.48	0.42	7.72	2.46
14.17	2.51	0.42	8.03	2.46
15.26	2.54	0.42	8.13	2.46
16.35	2.57	0.42	8.34	2.47
17.44	2.60	0.42	8.53	2.47
18.53	2.60	0.42	8.69	2.48
19.62	2.66	0.42	8.87	2.48
20.71	2.69	0.42	8.98	2.49
21.80	2.76	0.41	9.21	2.49
22.89	2.79	0.41	9.36	2.49
23.98	2.80	0.41	9.50	2.51
25.07	2.87	0.41	9.59	2.50
26.16	2.95	0.40	9.74	2.50
27.25	3.03	0.40	9.94	2.50
28.34	3.09	0.40	10.04	2.51
29.43	3.19	0.39	10.21	2.50
30.52	3.29	0.38	10.33	2.50
31.61	3.36	0.38	10.53	2.51
32.70	3.45	0.38	10.58	2.51
33.79	3.58	0.37	10.69	2.51
34.88	3.65	0.37	10.80	2.51
35.97	3.81	0.36	10.95	2.50
37.06	3.95	0.35	10.99	2.50
38.15	4.05	0.35	11.15	2.51
39.24	4.18	0.35	11.16	2.51
40.33	4.40	0.34	11.23	2.50
41.42	4.58	0.33	11.38	2.50
42.51	4.69	0.33	11.52	2.50
43.60	4.93	0.32	11.55	2.50
44.69	5.16	0.31	11.65	2.50
45.78	5.37	0.31	11.70	2.50

46.87	5.62	0.30	11.78	2.50
47.96	5.92	0.29	11.83	2.50

$M_{200} = 10^{8.5} M_{\odot}, \sigma/m = 14.62 \text{ cm}^2 \text{ g}^{-1}$

1.39	5.24	0.21	3.80	1.94
2.78	3.75	0.29	4.43	2.13
4.17	3.23	0.33	4.92	2.22
5.56	2.98	0.35	5.37	2.27
6.95	2.80	0.37	5.80	2.32
8.34	2.68	0.39	6.15	2.36
9.73	2.58	0.40	6.54	2.39
11.12	2.58	0.40	6.83	2.40
12.51	2.51	0.42	7.19	2.43
13.90	2.54	0.41	7.43	2.43
15.29	2.50	0.42	7.66	2.45
16.68	2.49	0.42	7.94	2.46
18.07	2.54	0.42	8.15	2.46
19.46	2.55	0.42	8.35	2.47
20.85	2.58	0.42	8.51	2.48
22.24	2.59	0.42	8.74	2.49
23.63	2.63	0.42	8.92	2.49
25.02	2.67	0.42	9.14	2.49
26.41	2.72	0.42	9.27	2.49
27.80	2.75	0.42	9.51	2.50
29.19	2.83	0.41	9.68	2.50
30.58	2.87	0.41	9.88	2.50
31.97	2.95	0.40	10.04	2.50
33.36	2.99	0.40	10.21	2.51
34.75	3.04	0.40	10.35	2.51
36.14	3.13	0.39	10.51	2.51
37.53	3.18	0.39	10.64	2.52
38.92	3.32	0.38	10.77	2.51

$M_{200} = 10^{8.5} M_{\odot}, \sigma/m = 18.60 \text{ cm}^2 \text{ g}^{-1}$

1.09	5.28	0.21	3.80	1.94
2.18	3.83	0.28	4.43	2.11
3.27	3.29	0.32	4.92	2.21
4.36	2.96	0.35	5.37	2.28
5.45	2.82	0.37	5.74	2.31
6.54	2.70	0.39	6.13	2.35
7.63	2.59	0.40	6.50	2.39
8.72	2.55	0.41	6.83	2.41
9.81	2.51	0.42	7.13	2.43
10.90	2.49	0.42	7.45	2.44
11.99	2.54	0.42	7.65	2.44
13.08	2.50	0.42	7.95	2.46
14.17	2.52	0.42	8.18	2.47
15.26	2.58	0.42	8.36	2.46
16.35	2.58	0.42	8.59	2.48
17.44	2.60	0.42	8.77	2.49
18.53	2.66	0.42	8.96	2.48
19.62	2.68	0.42	9.17	2.49

20.71	2.72	0.42	9.29	2.49	9.31	2.62	0.40	6.43	2.39
21.80	2.76	0.41	9.48	2.50	10.64	2.59	0.40	6.75	2.40
22.89	2.84	0.41	9.61	2.50	11.97	2.55	0.41	7.05	2.42
23.98	2.87	0.41	9.81	2.50	13.30	2.53	0.42	7.36	2.44
25.07	2.97	0.40	10.01	2.50	14.63	2.55	0.42	7.54	2.44
26.16	3.03	0.40	10.08	2.50	15.96	2.56	0.42	7.78	2.45
27.25	3.08	0.40	10.26	2.51	17.29	2.58	0.42	7.98	2.46
28.34	3.15	0.39	10.41	2.51	18.62	2.59	0.42	8.25	2.47
29.43	3.25	0.39	10.58	2.51	19.95	2.60	0.42	8.45	2.48
30.52	3.35	0.38	10.71	2.51	21.28	2.65	0.42	8.61	2.48
31.61	3.42	0.38	10.85	2.51	22.61	2.67	0.42	8.80	2.48
32.70	3.53	0.37	11.07	2.51	23.94	2.73	0.41	8.98	2.49
33.79	3.72	0.36	11.10	2.50	25.27	2.77	0.41	9.10	2.49
34.88	3.83	0.36	11.13	2.50	26.60	2.81	0.41	9.33	2.49
35.97	3.93	0.35	11.32	2.51	27.93	2.86	0.41	9.50	2.50
$M_{200} = 10^9 M_{\odot}, \sigma/m = 8.87 \text{ cm}^2 \text{ g}^{-1}$					29.26	2.91	0.40	9.71	2.50
1.96	5.36	0.21	3.81	1.92	30.59	3.00	0.40	9.84	2.50
3.92	3.81	0.28	4.43	2.12	$M_{200} = 10^{9.5} M_{\odot}, \sigma/m = 8.23 \text{ cm}^2 \text{ g}^{-1}$				
5.88	3.29	0.32	4.94	2.21	1.84	5.31	0.21	3.74	1.94
7.84	2.96	0.36	5.37	2.29	3.68	3.87	0.28	4.32	2.11
9.80	2.77	0.38	5.77	2.33	5.52	3.28	0.32	4.80	2.22
11.76	2.70	0.39	6.12	2.36	7.36	3.00	0.35	5.24	2.28
13.72	2.63	0.40	6.52	2.38	9.20	2.84	0.37	5.64	2.32
15.68	2.59	0.40	6.75	2.40	11.04	2.76	0.38	5.98	2.35
17.64	2.59	0.41	7.04	2.41	12.88	2.66	0.39	6.32	2.38
19.60	2.57	0.41	7.28	2.43	14.72	2.61	0.40	6.61	2.40
21.56	2.57	0.41	7.52	2.44	16.56	2.56	0.41	6.91	2.42
23.52	2.54	0.42	7.76	2.45	18.40	2.59	0.41	7.13	2.42
25.48	2.57	0.42	7.97	2.46	20.24	2.56	0.41	7.36	2.44
27.44	2.58	0.42	8.23	2.47	22.08	2.59	0.41	7.59	2.44
29.40	2.60	0.42	8.45	2.48	23.92	2.58	0.42	7.81	2.46
31.36	2.65	0.42	8.63	2.47	25.76	2.62	0.41	8.07	2.46
33.32	2.66	0.42	8.86	2.49	27.60	2.63	0.42	8.29	2.47
$M_{200} = 10^9 M_{\odot}, \sigma/m = 13.09 \text{ cm}^2 \text{ g}^{-1}$					29.44	2.62	0.42	8.57	2.48
1.33	5.36	0.21	3.81	1.93					
2.66	3.81	0.28	4.41	2.12					
3.99	3.26	0.33	4.90	2.22					
5.32	2.99	0.35	5.35	2.28					
6.65	2.83	0.37	5.74	2.32					
7.98	2.70	0.39	6.12	2.36					

TABLE III: The evolutions of the (2) core density $\rho_{c,T24}$, (3) core radius $r_{c,T24}$, (4) scale radius $r_{s,T24}$, and (5) intermediate region's inverted power-law index n_{T24} resulting from the χ^2_{cosmo} optimizations (for $r_{s,T24}$ we use the results of χ^2_{ideal} optimizations instead) with our density profile. The evolutions of different halos are presented separately. The halo characteristics are scaled according to Section III C while (1) times are displayed in physical units (Gyr).